OXFORD

Structural studies of ribosome from an anaerobic Bacteroidetes human pathogen *Porphyromonas gingivalis*

**Disha-Gajanan Hiregange[1], Sarit Samiya[1], Danuta Mizgalska[2], Efrat Ben-Zeev[3],
Miriam Waghalter[1], Andre Rivalta[1], K. Shanmugha Rajan[1], Yehuda Halfon[1],
Elinor Breiner-Goldstein[1], Igor Kaczmarczyk [1,2,4], Aneta Sroka[2,4], Masato Taoka [5], Yuko Nobe[5],
Toshiaki Isobe[5], Susanne Paukner[6], Ella Zimmerman[1], Anat Bashan [1], Jan Potempa[2,7],
Ada Yonath[1,*]**

[1]Department of Chemical and Structural Biology, Weizmann Institute of Science, Rehovot 7610001, Israel
[2]Department of Microbiology, Faculty of Biochemistry, Biophysics, and Biotechnology, Jagiellonian University, Krakow 30-387, Poland
[3]Nancy and Stephen Grand Israel National Center for Personalized Medicine, Mantoux Institute for Bioinformatics, Weizmann Institute of Science, Rehovot 7610001, Israel
[4]Doctoral School of Exact and Natural Sciences, Jagiellonian University, Krakow 30-387, Poland
[5]Department of Chemistry, Graduate School of Science, Tokyo Metropolitan University, Minami-Osawa 1-1, Hachioji-shi, Tokyo 192-0397, Japan
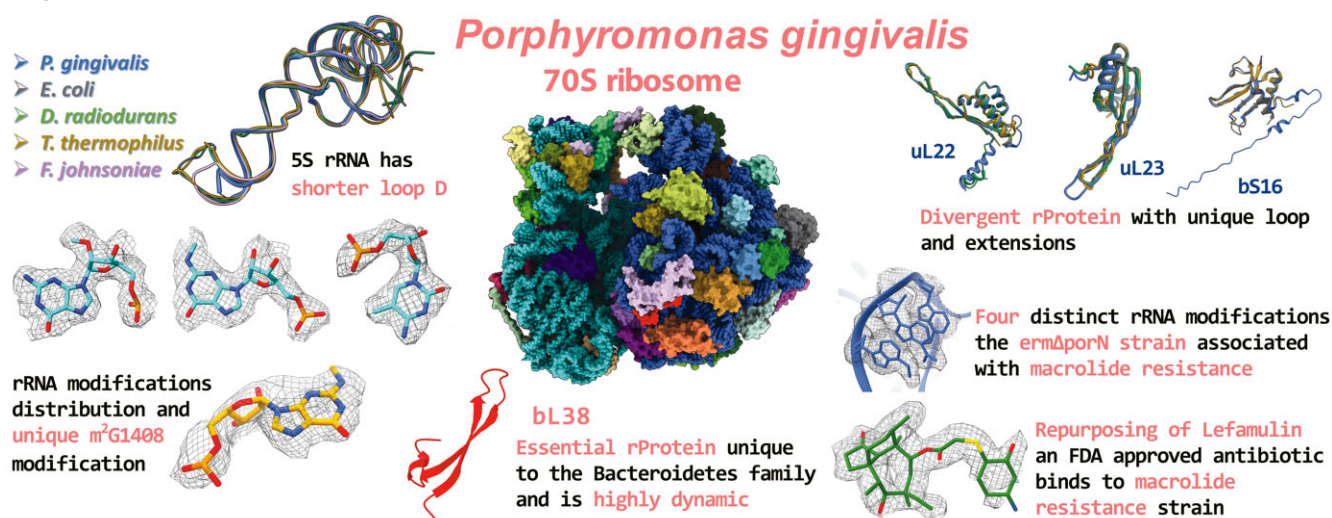[6]Nabriva Therapeutics GmbH, Vienna 1110, Austria
[7]Department of Oral Immunology and Infectious Diseases, University of Louisville, Louisville, KY 40292, United States
*To whom correspondence should be addressed. Email: ada.yonath@weizmann.ac.il

Abstract

Porphyromonas gingivalis, an anaerobic pathogen in chronic periodontitis, belongs to the Bacteroidota phylum and is associated with various virulence factors. Its antibiotic-resistant strains and its propensity to form biofilms pose a challenge to effective treatment. To explore therapeutic avenues, we studied the high-resolution cryogenic electron microscope structures of ribosomes from the wild-type *P. gingivalis* W83 and the macrolide-resistant mutant strain ermΔporN. The structural analysis revealed unique features primarily at the ribosome periphery. Together with the distinctive distribution of ribosomal RNA modifications, these findings offer insights into the therapeutical potential, such as creation of novel therapeutic compounds inhibiting the specific cellular functions of the *P. gingivalis* ribosomes. Moreover, the high-resolution structure of the ermΔporN ribosome in its complex with the approved antibiotic lefamulin suggests its repurposing against *P. gingivalis*. Furthermore, we provide a foundation for additional effective strategies to treat periodontitis and associated systemic diseases.

Graphical abstract

Introduction

Ribosomes are the universal cellular machines for synthesizing proteins according to the genetic instructions. Being vital for cell survival, ribosomes are the target of ∼40% of antibiotics in clinical use, which act mainly by binding to the ribosomes' functional centers [1, 2]. The worldwide dramatic increase in the pathogenic strains' resistance to antibiotics raises the need for novel strategies to combat them. The distinction between bacterial and eukaryotic ribosomes is the universal basis for antibiotic usage. Although species-specific effects of clinically relevant antibiotics are limited, certain characteristics, such as antibiotic resistance mechanisms, have been identified [3]. Furthermore, structural studies of ribosomes have shown minor, but significant, structural differences unique for several pathogenic bacteria, which could be explored for novel species-specific drug-binding targets [4–8]. Recent studies have shown that targeting peripheral species-specific features of ribosomal RNA (rRNA) can also inhibit ribosome activity, providing a promising foundation for developing novel non-conventional antibiotics [9, 10].

Porphyromonas gingivalis (PG) is an anaerobic gram-negative bacterium, a member of Bacteroidetes. It is found in oral cavities and is a concerning oral health issue with broader systemic implications. It is a key player in the development of periodontal disease, a chronic inflammatory condition affecting the gums and the supporting structures of the teeth. PG is known to cause the production of various proteases, including gingipains, which are thought to contribute to the pathogenesis of periodontitis by disrupting the normal functioning of host cells and tissues. These proteases can cleave several different proteins, including extracellular matrix components, host cell surface receptors, immune system molecules such as antibodies, and complement proteins. By functioning this way, they may interfere with important host defense mechanisms and promote the survival and growth of the bacterium within the host [11–13]. Recent studies illuminated the role of PG in contributing to a spectrum of systemic health issues, including cardiovascular, gastrointestinal tract, and respiratory tract diseases, as well as colorectal cancer [14–17]. Importantly, PG infection has recently been linked to Alzheimer's disease [18, 19]. These findings underscore the importance of implementing effective prevention and treatment strategies to mitigate the consequences of PG infection.

Antibiotic-resistant strains are frequently identified among clinical isolates of PG [20–23]. These, alongside the ability to form a biofilm, make the bacterium medically challenging to eradicate [24, 25]. Due to its high virulence and ability to cause severe health problems, deciphering the wild-type (WT) ribosome structure and its macrolide-resistant strain may be exploited to improve existing antibiotics and to develop new lead compounds against PG. To date, antibiotics such as tetracycline, macrolides, lincosamides, β-lactams, and nitroimidazoles have been suggested to treat PG-related infections [26–28]. However, their effectiveness has been compromised by the development of antibiotic-resistant strains. Furthermore, since PG is resistant to conventional treatment, it is a candidate for developing novel species-specific compounds to combat it.

The structure of the Bacteroidetes ribosome is characterized exclusively by the ribosome of *Flavobacterium johnsoniae* (FJ), a soil bacterium specialized in chitin and insoluble polymer degradation [29]. Significantly, the ribosome structure elucidated in our present study represents the first structural depiction of a pathogenic member of the Bacteroidota phylum within the human microbiome.

Our study focuses on the near-atomic cryogenic electron microscope (cryo-EM) structures of the ribosome from WT PG W83 (PG70SW83) and its isogenic ermΔporN mutant strain (PG70S-ermΔporN), the latter being avirulent due to inactivated type 9 protein secretion system (T9SS) [30]. In PG70S-ermΔporN, *ΔporN* gene is replaced by *erm* cassette, which encodes an adenosine methyl transferase that confers resistance to macrolide antibiotics (such as erythromycin), as well as lincosamides and streptogramin B antibiotics, by catalyzing the mono- or dimethylation of the *N6* position of single nucleotide adenine A2058 in the 23S rRNA [*Escherichia coli* (EC) numbering] [31, 32]. Our findings unveil the unique structural features of PG, which are primarily located at the ribosome periphery, along with specific rRNA modifications. These structural elements could serve as valuable targets for designing new compounds aimed at inhibiting ribosome activity.

Furthermore, we have elucidated the resistance mechanism of the macrolide-resistant mutant strain ΔporN carrying the *erm* cassette, which entails a single methylation and a dimethylation at the ribosomal macrolide binding site. Thus, aiming at repurposing existing antibiotic drugs against the macrolide-resistant PG ermΔporN strain, we have determined the cryo-EM structure of the PG ribosome in complex with lefamulin (PG50S-ermΔporN-lef), which is a pleuromutilin antibiotic that binds to the peptidyl transferase center (PTC) of the ribosome. It was recently developed and approved for treating community-acquired bacterial pneumonia caused by *Streptococcus pneumoniae*, *Staphylococcus aureus*, fastidious Gram-negative organisms, *Mycoplasma pneumoniae,* and *Chlamydophila pneumoniae* [33, 34]. Overall, this study holds significant implications for developing novel treatments against PG and presenting potential solutions for addressing antibiotic resistance.

Materials and methods

Purification of PG ribosomes

WT PG W83 and the isogenic ermΔporN mutant, obtained by replacing PorN coding sequence (CDS) with the *erm* cassette [35, 36], were grown in enriched trypticase soy broth (30 g/l) supplemented with yeast extract (5 g/l), L-cysteine (0.5 g/l), menadione (2 mg/l), and hemin (5 mg/l) in the chamber, at anaerobic conditions of 85% nitrogen, 5% hydrogen, and 10% carbon dioxide (Don Whitley Scientific, UK) at 37°C. Agar plates were supplemented additionally with 5% defibrinated sheep blood. PG cells of both W83 and ermΔporN strains were collected by centrifugation (15 min, $4000 \times g$) from cultures in late exponential growth phase (OD_{600} ∼1.0) and lysed in a lysis buffer [45 mM HEPES (pH 7.6), 100 mM KCl, 10 mM $MgCl_2$, 250 mM sucrose, 5 mM β-mercaptoethanol, 1:40 of rRNasin solution]. The cell lysate was then layered on a 1.1 M sucrose cushion [10 M Tris (pH 8), 14 mM Mg(OAc)$_2$, 60 mM KOAc, 6 mM β-mercaptoethanol, 1.1 M sucrose] and ultracentrifuged for 16.5 h in a Ti70 rotor at 4°C, $115\ 800 \times g$. The supernatant was discarded, and the pellet was then resuspended in Buffer C [20 mM HEPES–KOH (pH 7.6), 150 mM KOAc, 10 mM Mg(OAc)$_2$, and 5 mM β-mercaptoethanol]. The resuspension was then loaded on a 10%–40% sucrose gradient in the same

Buffer C and subjected to ultracentrifugation at 22 000 rpm for 15 h at 4°C on an SW28 rotor (Beckman). The peaks were collected using a gradient fractionator, flash-frozen in aliquots, and stored at −80°C.

Cryo-EM data collection and refinement for PG ribosomes

PG ribosomes (3.5 µl of 0.3 mg/ml 70S ribosome) were placed onto glow-discharged holey carbon grids coated by a continuous thin carbon film (Quantifoil Cu300 R2/2 + 2 nm C). Vitrobot Mark IV (Thermo Fisher Scientific) was used to blot and plunge-freeze the grids. Vitrobot parameters: sample volume 3.5 µl, blot time 2.5 s, wait time 30 s, and blot force −1. Titan Krios electron microscope (Thermo Fisher Scientific) operating at 300 kV was used to collect cryo-EM micrographs at liquid nitrogen temperature with K3 direct electron detector (Gatan Inc.) at a nominal magnification of 105K, with a pixel size of 0.842 Å/pixel. Defocus values ranged from -0.5 to -1.5 µm. RELION 3.1 [37, 38] was used for data processing. Motion correction was performed using Motioncor2 [39]. The contrast transfer function parameters were estimated using CTFFIND-3 [40]. Semiautomatic particle picking was followed by reference-free 2D classification and resulted in a particle count that was used for building a 3D initial model [41]. The particles were subjected to unsupervised 3D classification using a 60 Å low-pass filtered cryo-EM density map obtained from the initial 3D model as reference. The selected particles were used for auto-refinement. Following initial refinement, particles were subjected to Contrast Transfer Function (CTF) refinement, particle polishing, and 3D refinement to calculate a cryo-EM map. The resulting map was subjected to a cycle of multi-body refinement [42], producing maps at better resolution. The gold standard Fourier shell correlation (FSC) value criterion of 0.143 was used to determine average map resolutions, as implemented in RELION 3.1. Local resolution was estimated using Resmap [43].

Complex preparation of PG-ermΔporN ribosome with lefamulin

The PG50S-ermΔporN-lef was prepared by incubating 23 µl of the 0.3 mg/ml 70S ribosome in 10 mM HEPES (pH 7.6), 10 mM MgCl$_2$, 60 mM NH$_4$Cl, and 15 mM KCl buffer for 30 min at 26°C, and then 1.1 µl of 15 mg/ml lefamulin dissolved in distilled water was added and the mixture was incubated for 20 min on ice.

Model building of PG ribosome and its refinement

rRNA and ribosomal protein (rProtein) structures were built by combining template-guided and *de novo* model building in COOT [44]. The coordinates of *S. aureus* (PDBID 5LI0 [4]), *Deinococcus radiodurans* (DR) (PDBID 7A18 [45]), FJ (PDBID 7JIL [29]), *Thermus thermophilus* (TT) (PDBID 4W2E [46]) were used as a reference template for modeling with SWISS-MODEL [47] to obtain an initial model, which was then docked onto density maps using UCSF Chimera [48] and UCSF ChimeraX [49, 50]. The sequences of PG rRNA and rProteins were retrieved from NCBI and UniProt, respectively, with the specific IDs provided in Supplementary Table S1. rRNA modifications were manually modeled. Model refinement was performed using an iterative approach, including real-space refinement and geometry regularization in COOT, followed by real-space refinement using PHENIX

[51]. The final model was validated using MolProbity [52]. Sequence alignments were done using Jalview [53]. Figures were generated using UCSF Chimera [48] and UCSF ChimeraX [49, 50].

Deletion of RPL38 in PG

Genetic manipulations of PG were performed as previously described [54], and all constructs were built using the Gibson assembly method. A genomic deletion of *RPL38* was attempted through homologous recombination of a tetracycline resistance cassette flanked by a 778-bp upstream fragment and a 693-bp downstream fragment, carried by the vector *delRPL38_tet*. Clone selection was performed using 1 µg/ml tetracycline for 14 days. To rule out potential polar effects, the *RPL38* CDS was cloned under the strong promoter of the *RagAB* operon in a transient vector, *pRagAB-RPL38-TIO-tet*, and subsequently inserted into the conjugative plasmid *pT-COW*, which was modified to include an erythromycin resistance cassette for selection in PG, thereby named *pE-COW*. Conjugation was performed using EC S17-1 on a medium containing 5 µg/ml erythromycin. Positive clones were cultured, and genomic deletion of *RPL38* was attempted again using the *delRPL38_tet vector* (Supplementary Table S3).

Molecular dynamics simulations of bL38

Molecular dynamics (MD) simulation was performed using a DESMOND module by Schrödinger LLC software [55] (Schrödinger release 2024). The bL38 protein structure was predicted using AlphaFold3 [56] and immersed in the TIP3P solvent model orthorhombic box through the system builder panel. The solvated system was neutralized using counter ions and a physiological NaCl salt concentration of 0.15 M. OPLS4 force field was utilized. The simulation was 1000 ns using NPT assemble class at a temperature of 310.15 K and atmospheric pressure of 1.013 bar. Finally, to do a comprehensive examination, trajectories of simulated systems were generated. Using the Desmond module of the Schrödinger program, the following metrics were measured at various points along the trajectory: the root-mean-square deviation (RMSD), the root-mean-square fluctuation (RMSF), and the protein secondary structure elements (SSEs). RMSD displays the variation in a protein atom's structure during molecular simulation. A low RMSD indicates a more stable system in a simulation result. The RMSF is useful for characterizing local changes along the protein chain. SSE, such as alpha helices and beta strands, is monitored throughout the simulation.

Preparation of the PG rRNA and RNase digestion for MS analysis

The crude rRNA of PG was prepared from the ribosome fraction [using TRIZOL Reagent (Sigma as per manufacturer's instruction)]. 16S and 23S were purified by using reversed-phase liquid chromatography (LC) through a PLRP-S 4000A column (4.6 mm × 150 mm, 8 µm, Agilent Technologies) [57]. The rRNA were eluted with a 60-min gradient of 12.0%–14.0% (v/v) acetonitrile in 100 mM triethylammonium acetate (pH 7.0) and 0.1 mM diammonium phosphate from the column at a flow rate of 200 µl/min at 60°C. For 5S rRNA purification, the same buffer system was used with PLRP-S 300A column (2.1 mm × 150 mm, 3 µm, Agilent Technologies) and 60-min gradient of 11.2%–16% (v/v) acetonitrile at

a flow rate of 50 µl/min at 60°C. The eluates were monitored at A260.

Purified rRNA was digested with RNase T1 or A, and the resulting RNA fragments were cyanoethylated for labeling pseudouridine [58]. The RNA fragments were analyzed with a direct nanoflow Liquid Chromatography Mass Spectrometry (LC–MS) system as described [59]. The column was prepared with a fused-silica capillary (150 µm i.d. × 240 mm in length) packed with a reversed-phase material (Develosil C30-UG-3, 3 µm particle size; Nomura Chemical). The LC was performed at a flow rate of 200 nl/min using a 120-min linear gradient from 10% methanol to 7.6% methanol/9.8% acetonitrile in 10 mM triethylammonium acetate (pH 7.0). The eluate was sprayed online at −1.3 kV with the aid of a spray-assisting device to a Q Exactive Plus mass spectrometer (Thermo Fisher Scientific) in negative ion mode [60]. Ariadne [61] was used for database searches and assignment of MS/MS RNA spectra. The composite of PG rRNA sequences was used as a database. The following default search parameters for Ariadne were used: maximum number of missed cleavages, 1; variable modification parameters, two modifications including cyanoethyluridine, dihydrouridine, dimethyladenosine, hydroxycytidine, and methylation for any residue per RNA fragment; RNA mass tolerance, ±5 ppm; and MS/MS tolerance, ±20 ppm.

Susceptibility evaluation

Minimum inhibitory concentrations (MICs) of lefamulin, metronidazole, clindamycin, and imipenem were evaluated for clinical *Porphyromonas* spp. (n = 10) isolates including PG QC ranges for *Bacillus fragilis* ATCC 25285 and *B. thetaitaomicron* ATCC 29741, according to the reference agar dilution method as published by the Clinical Laboratory Standards Institute (CLSI) [62] using Brucella agar supplemented with 5% laked sheep blood. Briefly, test antimicrobials were diluted in 12 serial two-fold dilutions in Petri dishes containing molten Brucella agar, including supplements (final concentration range of 0.03–16 µg/ml). Upon solidification of the agar, the inoculum of PG isolates and QC isolates was applied to the agar surface with an inoculum-replicating apparatus, resulting in ∼10^5 CFU per spot. Plates were then incubated at anaerobic conditions at 35–37°C for 42–48 h, and MICs were read. The MIC is defined as the minimum concentration at which no growth or a marked reduction occurs in the appearance of growth observed compared with the growth control (no antimicrobial added). Based on the MIC values for individual isolates, we calculated the MIC_{50} and MIC_{90} values, which were defined as the concentrations at which 50% and 90% of tested isolates were inhibited, respectively.

Results

Overall structure of the *PG* ribosome

The structures of the various PG ribosomes were determined by using single particle cryo-EM techniques on purified intact ribosomes from WT PG W83 and its macrolide-resistant mutant strain ermΔporN with the *erm* cassette substituting the *porN* gene. For determining the PG70SW83 ribosome structure, the initial dataset, which included 129 576 particles, yielded a 3.0 Å resolution reconstruction of the entire ribosome. Subsequent refinement and Bayesian polishing improved the resolution to 2.63 Å for the whole ribosome. Multi-body refinement improved further the resolution to 2.6 Å for the large subunit (LSU), 3.01 Å for the small subunit (SSU) body, and 3.09 Å for the SSU head. For the PG70S-ermΔporN ribosome structure, the initial dataset that included 155 090 particles yields a 2.9 Å resolution reconstruction of the entire ribosome. Refinement and Bayesian polishing improved the resolution to 2.49 Å for the whole ribosome. Multi-body refinement further improved the resolution to 2.45 Å for the LSU, 2.77 Å for the SSU body, and 2.90 Å for the SSU head (Supplementary Fig. S1 and Table 1). The final cryo-EM maps and the refined atomic models are depicted in Fig. 1A and B. Notably, the local resolution of these reconstructions varied across the various ribosomal regions, with the core of the 50S subunit reaching a local resolution of ∼2.1 Å, indicating well-defined structures. In contrast, the ribosome flexible peripheral regions exhibit local resolution exceeding 5 Å, indicating higher structural variability (Supplementary Figs S2–S4). The structures account for ∼90% of rRNA components (16S, 5S, and 23S rRNA) and 19 SSU and 29 LSU rProteins (Fig. 1 and Supplementary Table S1). The cryo-EM structures of PG70SW83 and PG70S-ermΔporN show overall high similarity. Owing to its higher resolution, additional regions could be modeled in PG70S-ermΔporN compared to PG70SW83. Hence, we used PG70S-ermΔporN for structural analysis of species-specific rRNA and rProteins regions (Figs 2–4 and Supplementary Figs S5–S7).

Species-specific rRNA features of the PG ribosome

rRNA sequences of various organisms are used to study evolutionary relationships, since these are assumed to be of the ancient origins of all life forms. Although rRNA sequences may differ across organisms, the base-pairing schemes within these sequences typically form stem-loop structures [63]. The length and position of these stem loops lead to folding into internal three-dimensional rRNA structures that are similar across species. The 5S rRNA, which typically contains around 120 nucleotides in length, plays a significant role in the structure and function of the ribosome, which has been traditionally a model of choice in studies related to RNA structure and RNA–protein interactions due to its relatively small size, high abundance, and evolutionary conservation [64]. The positioning of 5S rRNA plays a unique role by acting as a molecular bridge connecting the various functional centers within the ribosome, thus facilitating the efficient and accurate process of protein translation.

Structural superimposition of PG70S ribosome on other bacterial ribosome structures determined by X-ray crystallography and Cryo-EM such as EC, DR, FJ, and TT ribosomes indicated a noticeably shorter PG70S loop D region of 5S rRNA (Fig. 2A–C). However, due to their local poor density, we were unable to model four nucleotide residues of the 5S rRNA at the tip of the loop D. This structural variation is significant because loop D is situated at the tip of the 5S rRNA and interacts directly with other ribosomal components, such as H39 and uL16. Our structure and those obtained by former studies indicate the proximity of loop D of 5S rRNA to two critical regions of 23S rRNA: domain II, involved in translocation, and domain V, involved in peptide bond formation. However, despite this proximity, the shorter loop D of 5S rRNA in PG70S does not interact extensively with H39 and interacts only minimally with uL16, unlike in EC ribosomes where such interactions are prominent [65].

Table 1. Cryo-EM data collection and model refinement

Subunit	PG70SW83	PG70S-ermΔporN	PG50S-ermΔporN-lef
Data collection			
Microscope		Titan Krios	
Camera		Gatan K3	
Voltage (kV)		300	
Magnification		105 000	
Pixel size (Å/pixel)		0.842	
Defocus range (μm)		(-0.5 to -1.50)	
Total dose (e/Å^2)		45	
Micrographs collected	5341	2402	4440
Refinement			
Number of particles (autopicked)	154 584	230 744	250 705
Number of particles (used for 3D reconstruction)	129 576	155 090	223 396
Resolution (Å; at FSC = 0.143)	3.0	2.9	2.5
CC (model to map fit)	0.86	0.90	0.87
Bonds (Å)	0.005	0.005	0.007
Angles (°)	0.690	0.679	0.817
Chirality (°)	0.039	0.041	0.040
Planarity (°)	0.005	0.005	0.007
Clashscore	4.16	4.65	4.32
MolProbity score	1.73	1.68	1.91
Rotamer outliers (%)	1.80	1.43	3.17
Ramachandran favored (%)	95.14	95.34	95.46
Ramachandran allowed (%)	4.86	4.66	4.51
Ramachandran outliers (%)	0.00	0.00	0.03
Correct sugar pucker (%)	99.52	99.45	99.20
Correct backbone conformation	84.35	85.88	87.74

Notably, uL16 extends to the A-site of the PTC. In EC ribosomes, 5S rRNA interacts directly with uL16, unlike in PG70S ribosomes, where such interaction is lacking (Fig. 2D). Nevertheless, despite this "hole," PG70S ribosomes maintain their functionality (Supplementary Fig. S5A).

Structural comparisons of PG 23S rRNA and 16S rRNA with the same features of DR, FJ, and TT rRNA reveal primary distinctions in the ribosomal subunit's outer regions. Specifically, these differences are most noticeable in helices h9, h17, and H28. In the case of PG70S, helix h9 and h17, located at the periphery of the small subunit, are extended compared to the same helices in TT. The extended conformation in PG70S leads to an interaction of rProtein uS17 with h9 and bS16 with h17, which does not occur in the TT ribosome (Supplementary Fig. S5B and C). In contrast, PG70S H28, situated at the periphery of the large ribosomal subunit, is shorter than its corresponding feature in DR, FJ, and TT, thus disrupting the interaction with rProtein uL4 (Supplementary Fig. S5D). These structural differences may have some functional consequences, which are currently still undefined but may be tested by targeting them specifically.

Divergent rProteins of the PG ribosome
While rProteins are known for their structural conservation across the bacterial domain, a closer examination of the proteins of the PG ribosome and their comparisons to those in EC, DR, FJ, and TT ribosomes reveal some intriguing structural differences. The structural comparison revealed that most rProteins in PG maintain structural similarity to their counterparts in EC, DR, and TT ribosomes, despite some variations in their N- or C-terminal extensions.

In PG70S ribosome, we could model bS22 that is annotated as a hypothetical protein (GenBank: AAQ66340.1) (Fig. 3A), comprising 30 amino acids that occupy a similar position as reported in the FJ ribosome [29]. Comparative analysis hints that although bS22 may differ in sequence, its folding resembles bS22 in *Mycobacterium smegmatis* [66, 67] and eL41 in *Homo sapiens* [68] (Fig. 3B and C). bS22 is located between helices h44 and h45 of the 16S rRNA and interacts with helix H70 of the 50S subunit, suggesting potential bridging interactions with both the 23S and 16S rRNA (Fig. 3D). bS22's role seems crucial in potentially stabilizing h44, which undergoes significant conformational changes during transfer RNA (tRNA) translocation [69], and its interaction with h45 may influence elements near the mRNA exit site [66, 67, 70]. Moreover, the C-terminus of bS22 interacts with H70 in the 23S rRNA of the 50S subunit, potentially bolstering intersubunit contacts and providing stability to PG70S. In this context, the finding of bS22, which connects the small and large subunits, renders the PG akin to eukaryotes, where such bridging is a characteristic feature (eB14). Positioned at the 30S and 50S subunit interface near the mRNA channel, bS22 could facilitate the recruitment of additional ribosomal factors during translation regulation. Notably, bS22's proximity to the aminoglycoside binding sites of h44 in the decoding center (DC) suggests a possible role in modulating the aminoglycoside binding pocket (Fig. 3E). A recent study on *M. smegmatis* hints that strains lacking the bS22 gene can display enhanced susceptibility to kanamycin compared to WT strains, suggesting a potential involvement of bS22 in modulating the aminoglycoside binding pocket in the DC of the 30S subunit [71].

In PG70S-ermΔporN and PG50S-ermΔporN-lef ribosomes, we were able to identify the density for bL38, a novel

Figure 1. (**A**) Front and back views of the cryo-EM map of the PG ribosome colored according to the structure shown in panel (B). The map contour level is 1.9σ. (**B**) The atomic structure of the PG ribosome is shown in the same front and back views as in panel (A). rRNA is shown as atoms colored in blue, whereas rProteins are shown as space-filling models. (**C**, **D**) Representative segments of the PG cryo-EM map together with the associated atomic models of a segment from the uL2 and a base pair of 23S rRNA. The map contour level is 1.9σ.
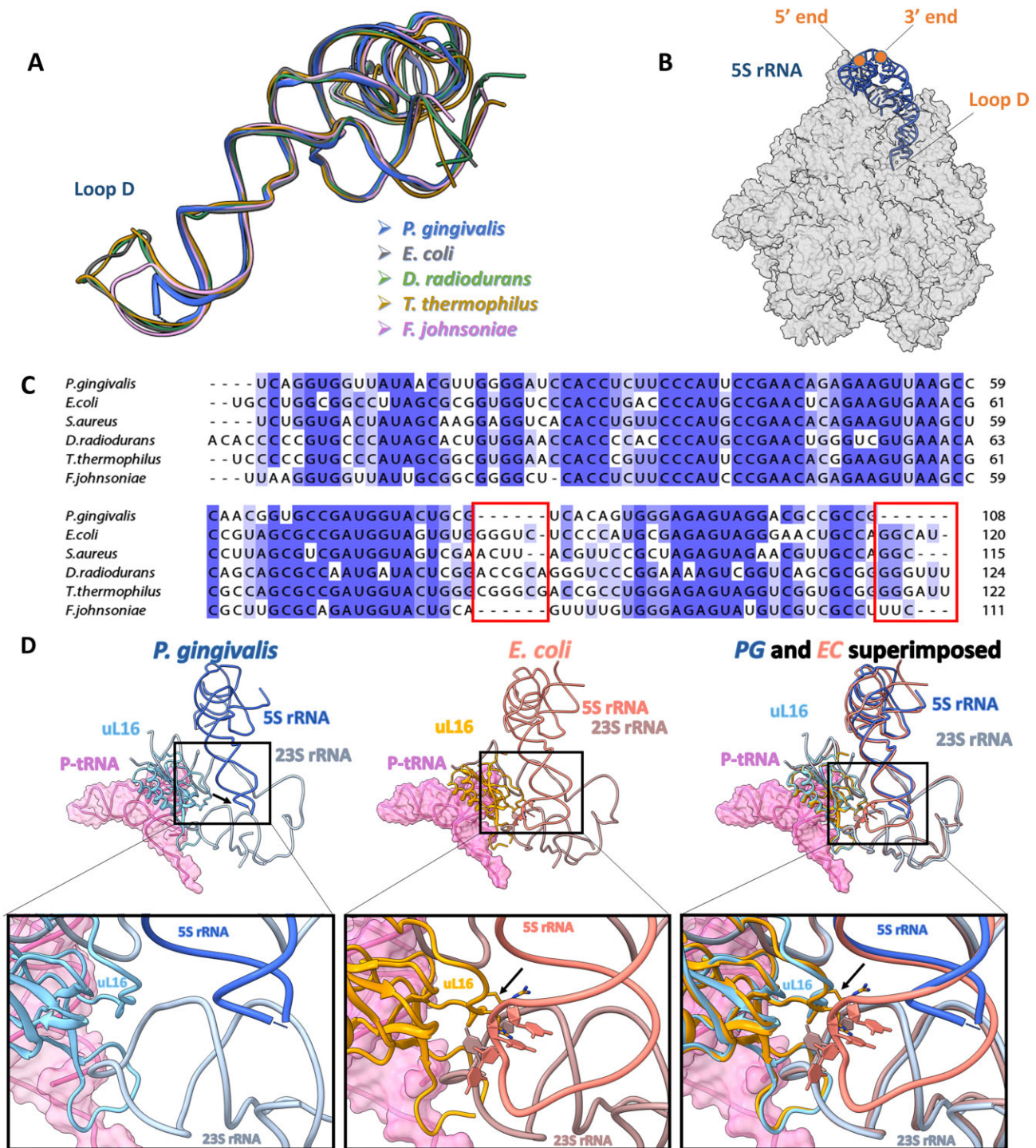
Figure 2. Shorter 5S rRNA of PG. (**A**) Ribbon representation of PG 5S rRNA (shown in blue) is superposed on 5S rRNA of EC, TT, FJ, and DR (PDBIDs: 7K00, 4W2E, 7JIL, and 7A18, shown in gray, golden, pink, and green, respectively). (**B**) The spatial position of 5S rRNA (illustrated in blue) within the 50S subunit. (**C**) Multiple sequence alignment between 5S rRNA of PG, EC, TT, and DR. The red rectangle marks the differences in the rRNA sequence of PG. (**D**) Loss of interaction between 5S rRNA, 23S rRNA, and uL16 of PG (shown in shades of blue) compared to EC (shown in shades of salmon).

protein found exclusively in the Bacteroidota phylum, initially identified in FJ (Supplementary Fig. S7C) [29]. While we were able to model the C-terminus region of the protein from Gly14 to Lys49, no clear density was observed for the first 13 residues of the N-terminus (Fig. 3F). However, due to insufficient density and local lower resolution of the EM map in this region, we could not model bL38 in PG70SW83. Since bL38 interacts with H95, H97, and uL6 of the 50S subunit and is located

on the periphery of the ribosome, it may engage with other ribosomal factors, as well as non-ribosomal cellular components, rendering it accessible and a potential target for drug intervention.

Furthermore, rProtein uS4 of the PG70S-ermΔporN ribosome exhibits a shorter loop (indicated by an arrow in Fig. 4A), resulting in the absence of interactions with 16S rRNA in contrast to its counterparts in FJ, EC, and TT ribosomes
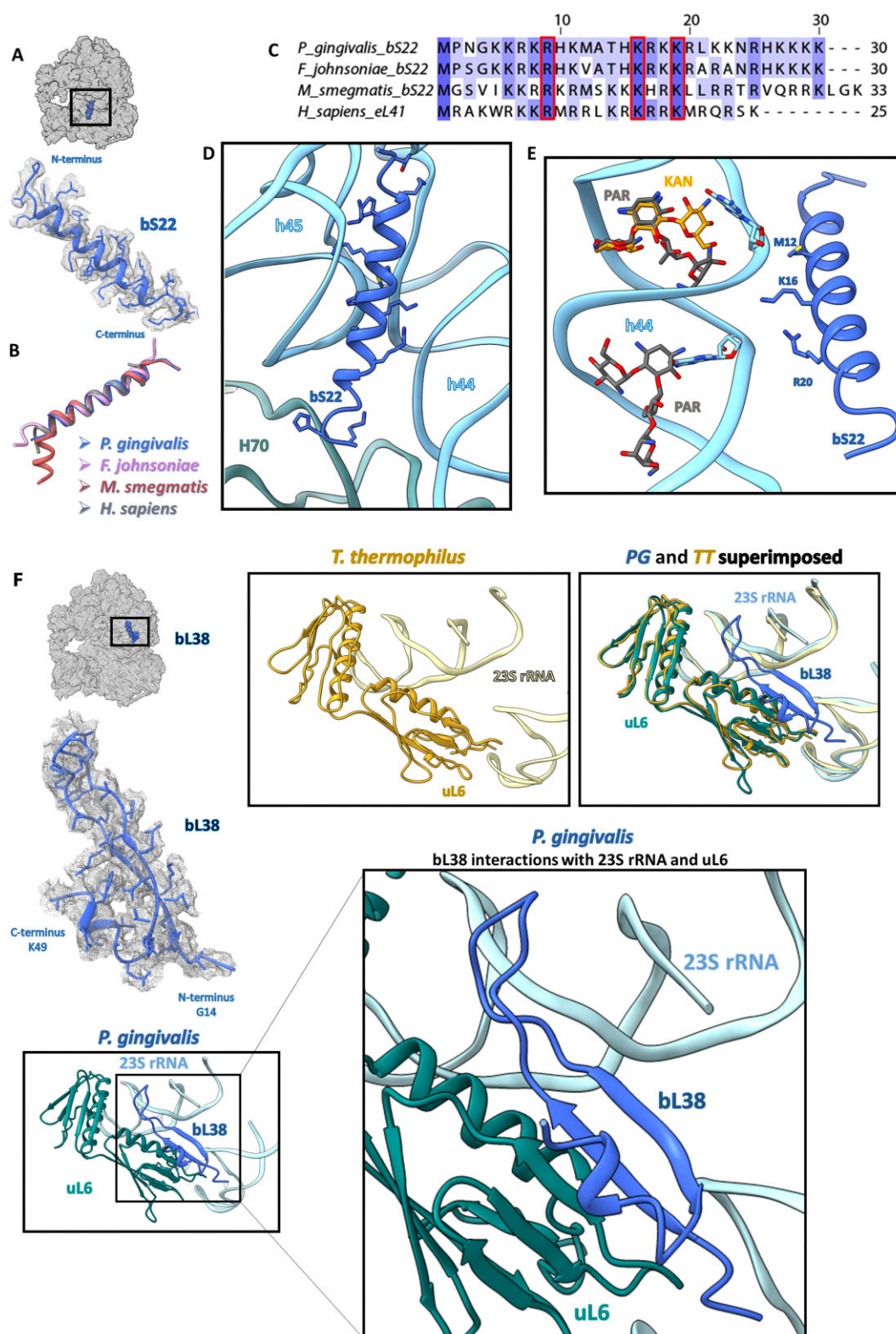
Figure 3. Divergent rProteins in the PG ribosome. (**A**) The modeled amino acid sequence for bS22 is fitted into the density of the cryo-EM map. (**B**) Superposition of bS22 of PG (shown in blue) to a structurally similar protein of FJ, MS, and HS (PDBIDs: 7JIL, 5O61, and 8G6J, shown in pink, light red, and gray, respectively). (**C**) Multiple sequence alignment of bS22 and the structurally similar protein of FJ, MS, and HS. (**D**) Interaction of bS22 with h44 and h45 of 16S rRNA. (**E**) Superposition of kanamycin (KAN, PDB1D-8EV7) and paramomycin (PAR, PDB1D-6AZ1) onto 16S rRNA of PG ribosome and bS22 interaction with it. (**F**) The model of bL38 is shown as fitted into the EM density map. Specific rProteins of PG (shown in blue) are superposed on the equivalent rProteins of TT (PDBIDs: 4W2E, shown in gold). Its specific interactions with their neighboring rRNA are also shown. The spatial positions of both rProteins (shown in blue) are shown on the gray ribosome silhouette.
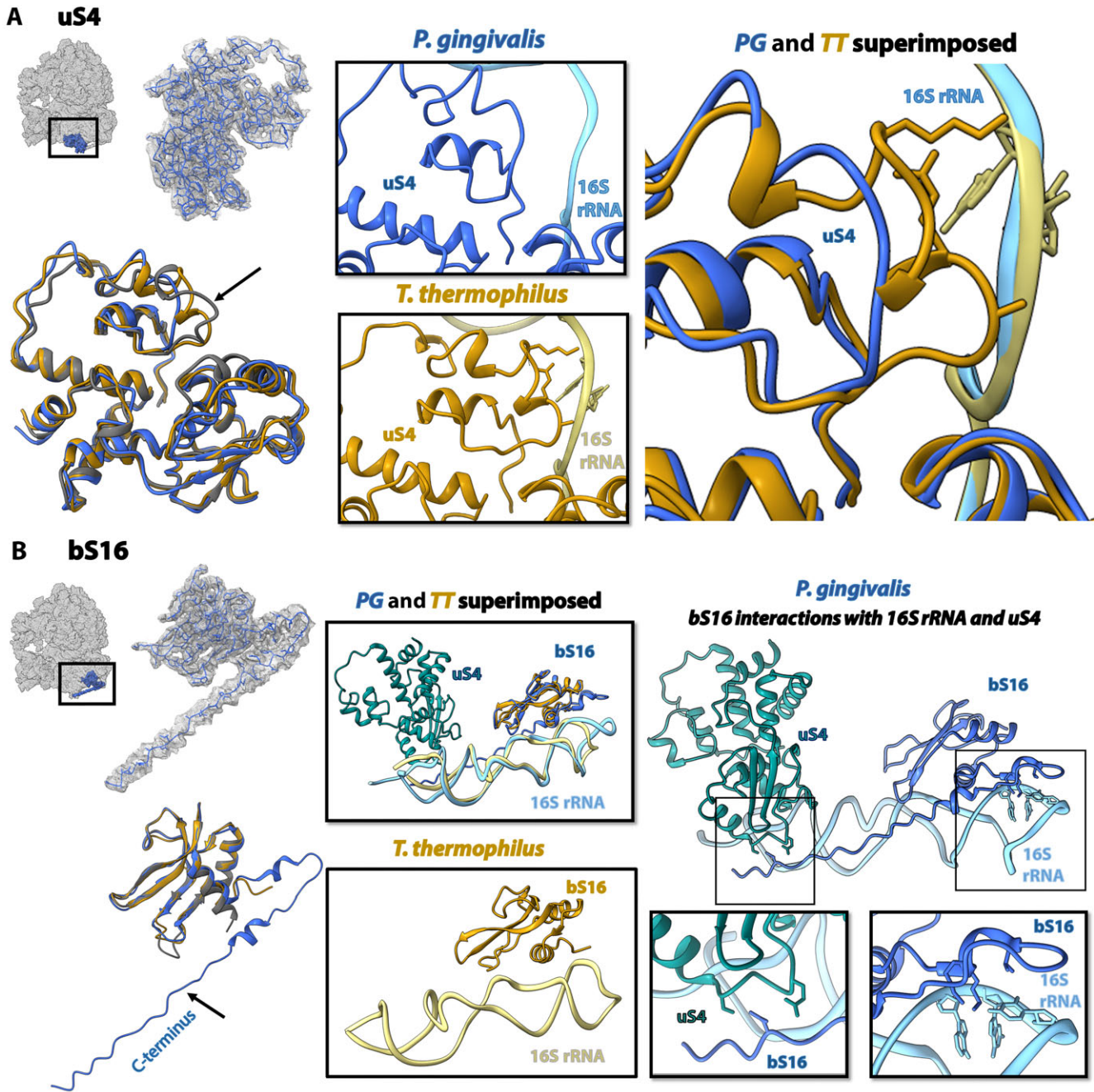
Figure 4. Structural variability within the PG rProteins. Specific rProteins of PG (shown in blue) are superposed on the equivalent rProteins of EC and TT (PDBIDs: 7K00 and 4W2E, shown in gray and gold, respectively), and their specific interactions with their neighboring rRNA are shown. The spatial position of both rProteins (shown in blue) is shown on the gray ribosome silhouette. (**A**) uS4. (**B**) bS16. An arrow points at a unique loop in PG uS4 and bS16.

(Fig. 4A and Supplementary Figs S7E and S8D). Moreover, ~100 extra residues of the C-terminus of rProtein bS16 of PG70S-ermΔporN are located at the periphery of the small subunit, a feature absent in the EC and TT ribosome. This extended C-terminus that exists in the family of Bacteroidota creates a unique interaction between 16S rRNA and rProtein uS4, a specific feature of the Bacteroidota ribosome (Fig. 4B and Supplementary Fig. S8E) (this loop is part of the FJ bS16 rProtein sequence but was not modeled in the structure of FJ [29]). Both uS4 and bS16 play crucial roles in the 30S subunit ribosome assembly, with uS4 initiating the assembly process [72]. Therefore, this unique bS16–uS4 interaction

appears to provide additional stability during the 30S subunit assembly in PG.

The PG70S rProtein uL22 N-terminus includes 17 additional residues, compared to EC, DR, FJ, or TT ribosomes, which form a helical structure. This elongated N-terminus, on the ribosomal surface, is distinct from the longer non-helical N-terminus in DR and the semi-helical N-terminus in FJ (Supplementary Fig. S7D). It interacts with the features of 23S rRNA that are located on the surface of the 50S subunit and inserted between the 23S rRNA helices H25 and H47, forming hydrogen bonds within this helical region. In addition, a unique extended loop, including positions 79–87,

is located at the subunit surface (indicated by an arrow in Supplementary Fig. S6A). This region presents a promising target for developing novel specific drugs against PG, as uL22 is positioned near the polypeptide exit tunnel on the external surface of the subunit (Supplementary Figs S6A and S8A).

In addition, rProtein uL23 PG70S features an unusual extended loop between residues 65–70 within the subunit interior (indicated by an arrow in Supplementary Fig. S6B). This elongated loop leads to unique interactions with the 23S rRNA, distinguishing it from its counterparts in EC, DR, and TT ribosomes (Supplementary Figs S6B and S8B) (in the FJ ribosome, this loop was not modeled; therefore, we could not show the comparison). Sequence-wise, an extended loop is part of its uL23, but its amino acid sequence is not conserved (Supplementary Fig. S8B).

Additionally, uS14 exhibits a shorter loop compared to the EC counterpart and an extended loop compared to the TT counterpart. This loop is part of the FJ uS14 rProtein sequence but was not modeled in the structure of FJ (Supplementary Figs S7A and S8F). Also, uL6 showed the presence of an extended loop compared to its counterparts in EC, DR, and TT ribosomes (Supplementary Figs S7B and S8C).

We also could model 34 amino acid residues from the complete RaiA protein (Ribosome associated inhibitor A; 400 aa) (Supplementary Fig. S7F), which seems to occupy the same position as hpf in the SA 100S dimer (PDBID 5NGM). Although the sequence is not highly homologous, the domain that binds in the tRNA binding site is structurally similar to hpf [73].

Studies have shown that over 200 bacterial genomes showed substantial variability in Shine–Dalgarno (SD) sequence usage [74]. Interestingly, some lineages, including Bacteroidetes and a subset of Cyanobacteria (with a few exceptions), were observed to lack SD sequences entirely (a finding confirmed in later studies [75–77]), while retaining the canonical anti-Shine–Dalgarno (ASD) sequence at the 3′ end of their 16S rRNA [78, 79]. A recent study revealed that the ASD sequence at the 3′ end of the 16S rRNA is maintained and stabilized by bS21, bS18, and bS6 on the 30S platform [29]. Although the 3′ end of the 16S rRNA in PG70S was not fully modeled due to poor EM density, the proteins that stabilize and sequester the 3′ end of 16S rRNA exhibited structural similarities to their FJ counterparts but not to their EC and TT counterparts, suggesting a similar mechanism of ASD inhibition (Supplementary Fig. S7G and H).

These structural distinctions between PG rProteins and other species, especially those of human pathogens, provide insights into the unique features of the PG ribosome and may serve as potential targets for developing novel species-specific drugs against PG.

bL38 is an essential and conformationally dynamic rProtein

Attempts to delete *RPL38* through homologous recombination using the *delRPL38_tet* vector did not yield any viable colonies, even after three independent experiments with tetracycline selection for 14 days. This strongly suggested that *RPL38* is an essential gene in PG, as its deletion was not tolerated under the tested conditions.

To rule out the possibility of a polar effect on downstream genes, a cytoplasmic copy of *RPL38* was introduced under the control of the strong *RagAB* operon promoter in the *pE-COW* plasmid, allowing constitutive expression of *RPL38* indepen-

dent of its genomic locus. Following the successful selection of PG clones carrying *pE-COW*, a second round of genomic deletion using the *delRPL38_tet vector* was performed. This time, viable colonies were obtained, and PCR verification confirmed the successful deletion of the genomic *RPL38* locus. The ability to delete *RPL38* only when a plasmid-expressed copy was present confirms that rProtein bL38 is essential for the survival of PG (Fig. 5A and Supplementary Fig. S11A).

Furthermore, to investigate the structural stability and dynamic behavior of the bL38 protein from PG, we performed MD simulations and analyzed both its SSE and residue-wise flexibility.

The secondary structure analysis revealed that bL38 maintains a predominantly β-strand architecture, with minimal fluctuations in the core structural elements, while the loop and terminal regions exhibit higher flexibility (Fig. 5B). The time-resolved SSE analysis demonstrated that the β-strands remained stable throughout the simulation, whereas transient structural transitions were observed in the loop and terminal regions. The overall SSE content fluctuated around a steady-state value, suggesting that bL38 attains an equilibrium conformation during the simulation. The clustering of representative structures extracted at different time points highlights the progressive reorganization of the flexible termini (Fig. 5C and D), particularly the N-terminal Met1 and C-terminal Lys49, which undergo substantial movement relative to the central β-sheet.

To further quantify local flexibility, we analyzed the RMSF of individual residues throughout the simulation (Supplementary Fig. S11B and C). Peaks in the RMSF profile correspond to highly flexible regions, with the highest fluctuations observed in the N- and C-terminal residues. In contrast, residues within the β-strands displayed lower RMSF values, consistent with their role in maintaining the protein's structural integrity. Comparison with secondary structure assignment indicates that loop regions exhibit significantly higher fluctuations than the more rigid α-helical and β-strand elements.

Together, these results suggest that bL38 maintains a stable β-strand architecture while allowing for conformational flexibility in the loop and terminal regions. This dynamic behavior may play a role in its interactions with ribosomal components or its functional adaptability within the ribosome of PG.

rRNA modifications in the PG 70S ribosome

Numerous studies have highlighted the essential role played by modified rRNA in both catalytic activity and ribosome biogenesis [80, 81]. Structural studies of ribosomes have illuminated the importance of rRNA modifications in upholding the integrity and functionality of bacterial ribosomes [82, 83]. These rRNA modifications are strategically positioned in or around key functional sites, encompassing the peptide exit tunnel, regions where mRNA and tRNA interact, and the PTC [82, 84]. Furthermore, rRNA modifications influence the conformation of pockets where antibacterial agents bind [82]. In prokaryotic ribosomes, the number of modified nucleotides within rRNA is generally limited compared to the abundance of modifications in eukaryotic ribosomes. While rRNA modifications are prevalent across different species, their specific chemical composition and positions are less conserved.

In the PG ribosome, mass spectrometric analysis has revealed 31 rRNA modifications, among those 18 in the LSU
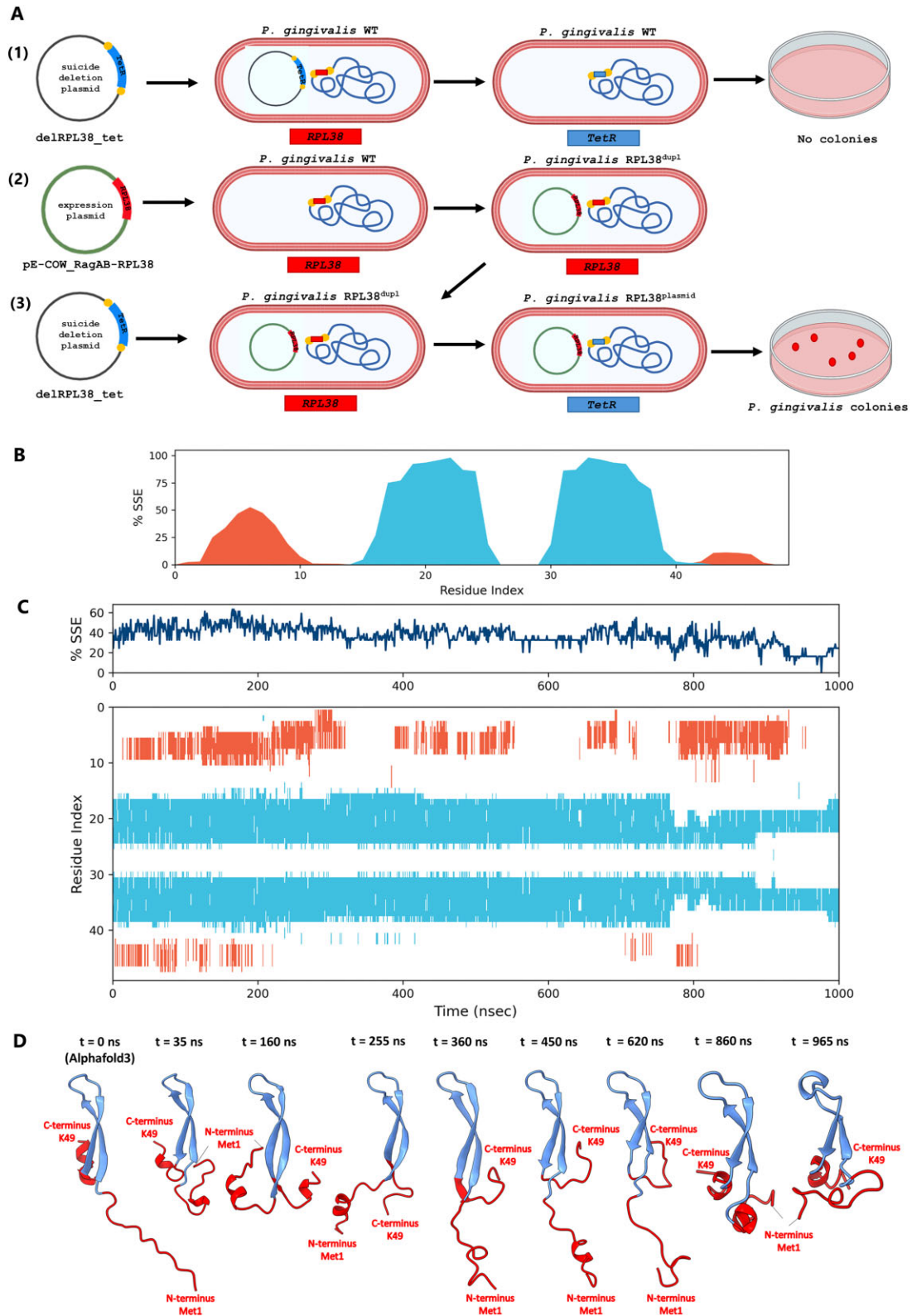
Figure 5. bL38 is an essential rProtein and conformationally dynamic. (**A**) Schematic representation of genetic experiments confirming bL38's essential nature. (1) Deletion of RPL38 gene resulted in no viable colonies. (2) Introducing an expression plasmid with a second RPL38 gene copy resulted in colonies with gene duplication. (3) Subsequent deletion of a genomic copy of RPL38 gene resulted in viable colonies proving no adverse polar effects of undertaken deletion strategy. (B–D) SSE of bL38 during 1000 ns MD simulation at 37°C. (**B**) The plot represents SSE distribution by residue index throughout the protein structure. Percentage of the total SSE is 37.08, and the rest of the protein is unstructured. (**C**) The stability of SSE over time. The top panel shows the total percentage of SSE throughout the simulation. The bottom panel maps the SSE assignment per residue as a function of time, highlighting regions of structural stability and transitions. (**D**) Cluster representative snapshots of the protein at different time points from the MD trajectory. The protein backbone is colored according to secondary structure, with beta strands in blue and flexible regions in red. The structural evolution over time illustrates conformational changes and potential unfolding or folding transitions.

and 13 in the SSU. Among those, cryo-EM analysis has enabled clear visualization of 25 of the rRNA modifications, 15 in the LSU and 10 in the SSU. Notably, some rRNA modifications, such as pseudouridine (Ψ) residues, could not be directly visualized by cryo-EM due to similar geometry with uridine. However, their identification by mass spectrometry and the presence of a stabilizing water molecule that forms a hydrogen bond between the Ψ residue and the phosphate backbone of the rRNA made their modeling into the 3D ribosome structure possible (Fig. 6 and Table 2).

Many of these rRNA modifications in PG (although not all) are situated within the interior of the ribosome rather than at its outer periphery. These are localized within and around functional regions such as the PTC, the DC, and the nascent protein exit tunnel (Fig. 6E).

For instance, overlaying the structure of the PG70S ribosome with bound tRNA revealed a potential interaction between the Gm2252 rRNA modification of LSU and the P-site tRNA during translation (Fig. 6F). Also, the methyl group of m^2G965 forms contacts with RaiA, an auxiliary ribosome subunit interface protein (Fig. 6G). Notably, a similar interaction is observed in the TT ribosome [84]. Lang *et al.* suggested that RaiA-bound inactive 70S ribosomes form intact and reactivable sleeping ribosome pools [85]. RaiA, identified as a ribosome-associated protein, operates under conditions similar to Rmf (ribosome modulation factor) and hpf (hibernation promoting factor) [86]. While the latter two factors induce the dimerization of vacant 70S ribosomes into inactive 100S ribosome dimers during ribosome hibernation in stationary phase [87], RaiA predominantly binds to free 70S monosomes [86, 88]. RaiA plays a protective role by preventing the degradation of 70S ribosomes [89, 90]. Additionally, it hinders tRNA binding to the ribosomal A site, both in a cell-free translation system [91] and during cold shock [92]. These contacts suggest that m^2G965 rRNA modification may play significant roles for both the ribosome affinity for the P-site tRNA (Fig. 6I) and its interactions with ribosome-associated proteins. Consequently, this could impair the ribosome's ability to respond to stress and stationary phase conditions during translation.

Additionally, many modifications in the SSU of PG70S ribosomes are clustered within the mRNA channel. Notably, the methyl groups of m^4C1400 and m^3U1487 establish contacts with the mRNA (Fig. 6H), indicating their potential significance in facilitating the proper accommodation of mRNA within the ribosome.

Furthermore, we observed that compared to other bacterial ribosomes, h44 of the DC of the ribosome contains a higher number of modified nucleotides, among which the m^2G1408 rRNA modification has not been reported to date in any other bacterial ribosome except in archaeal ribosome [93]. Remarkably, it is located in the vicinity of the aminoglycoside binding pocket of the 30S subunit (Fig. 6J) and might affect the affinity of antibiotic binding to PG ribosome.

Macrolide resistance mechanism of the PG ermΔporN mutant strain

PG employs a secretion system known as the T9SS, which enables the translocation from the periplasm across the outer membrane cell surface and extracellular virulence factors, specifically cysteine proteases referred to as gingipains [94]. Within this secretion system, PorN is a crucial component. However, in the ermΔporN modified strain of PG, the PG_0266 gene (which encodes PorN) was replaced with the *erm* cassette, which resulted in resistance to macrolide antibiotics and disruption of gingipains secretion [35]. The *erm* cassette encodes an adenosine methyltransferase that provides resistance to macrolide, lincosamide, and streptogramin B antibiotics by methylating the *N6* position of adenine A2058 in the 23S rRNA [31, 32]. However, by MS analysis for the identification of rRNA modifications of the PG70S-ermΔporN ribosome, four rRNA modifications were confirmed, namely A2057, A2058, A2059, and A2060 (EC numbering used throughout, which corresponds to PG numbering, is A2067, A2068, A2069, and A2070) (Supplementary Fig. S9). All of them are located within the exit tunnel entrance and are specific to this strain. Examining the cryo-EM maps, three of these modifications were visualized and subsequently modeled into the three-dimensional structure of the PG70S-ermΔporN ribosome (Fig. 7 and Table 2).

Additionally, the MS analysis revealed the specific modification rates for these residues. A2057 has a modification pattern of 48% A, 46% m^6A (methyladenine), and 6% m^6_2A (dimethyladenine). For A2058, the modification pattern consisted of 11% m^6A and 89% m^6_2A. However, the modification rates for A2059 and A2060 were relatively low (Supplementary Fig. S9 and Supplementary Table S2). Given the known bacterial macrolide binding site [45, 95], we could superimpose erythromycin into its respective bacterial binding site. This allowed us to illustrate how the rRNA modifications of A2058 and A2059 (the primary anchors for macrolide binding) introduce steric hindrance, thus affecting the binding of macrolide antibiotics, and, consequently, led to the emergence of macrolide resistance in the PG ermΔporN strain potentially through a mechanism similar to that previously observed in the TT ribosome [31].

Repurposing of the pleuromutilin antibiotic, lefamulin, against the PG ermΔporN strain

Pleuromutilins, which were discovered as inhibitors of *S. aureus* in 1951, are natural products produced by the *Pleurotus* genus [96]. These compounds feature a tricyclic mutilin core, a *C21* keto group, and various *C14* extensions. Studies have shown that pleuromutilin derivatives function by inhibiting bacterial protein biosynthesis through binding to the PTC at the A- and P-sites [97–102]. Lefamulin, developed by Nabriva Therapeutics, received approval from the US Food and Drug Administration (FDA) to be used in the United States in 2019 [34]. Importantly, lefamulin is the first pleuromutilin antibiotic to be utilized for the systemic treatment of bacterial infections in humans [103].

Since the PG ermΔporN strain is macrolide resistant, initially, we aimed to find an existing antibacterial drug that may bind to a different ribosomal site and inhibit this resistant strain. Thus, we determined the cryo-EM structure of the PG50S-ermΔporN in the complex with lefamulin (PG50S-ermΔporN-lef). In this complex structure, lefamulin binds at the PTC (Fig. 8A and C). The tricyclic mutilin core obstructs the A-site, while its 4-amino-2-hydroxy-cyclohexyl-sulfanyl-acetyl *C14* extension points into the P-site. This binding scheme disrupts the accommodation of the tRNA at both the A- and P-sites, in agreement with the inhibition mechanism found for DR [104, 105], HH [106], and SA [33]. The structures of lefamulin in complex with PG50S-ermΔporN-lef
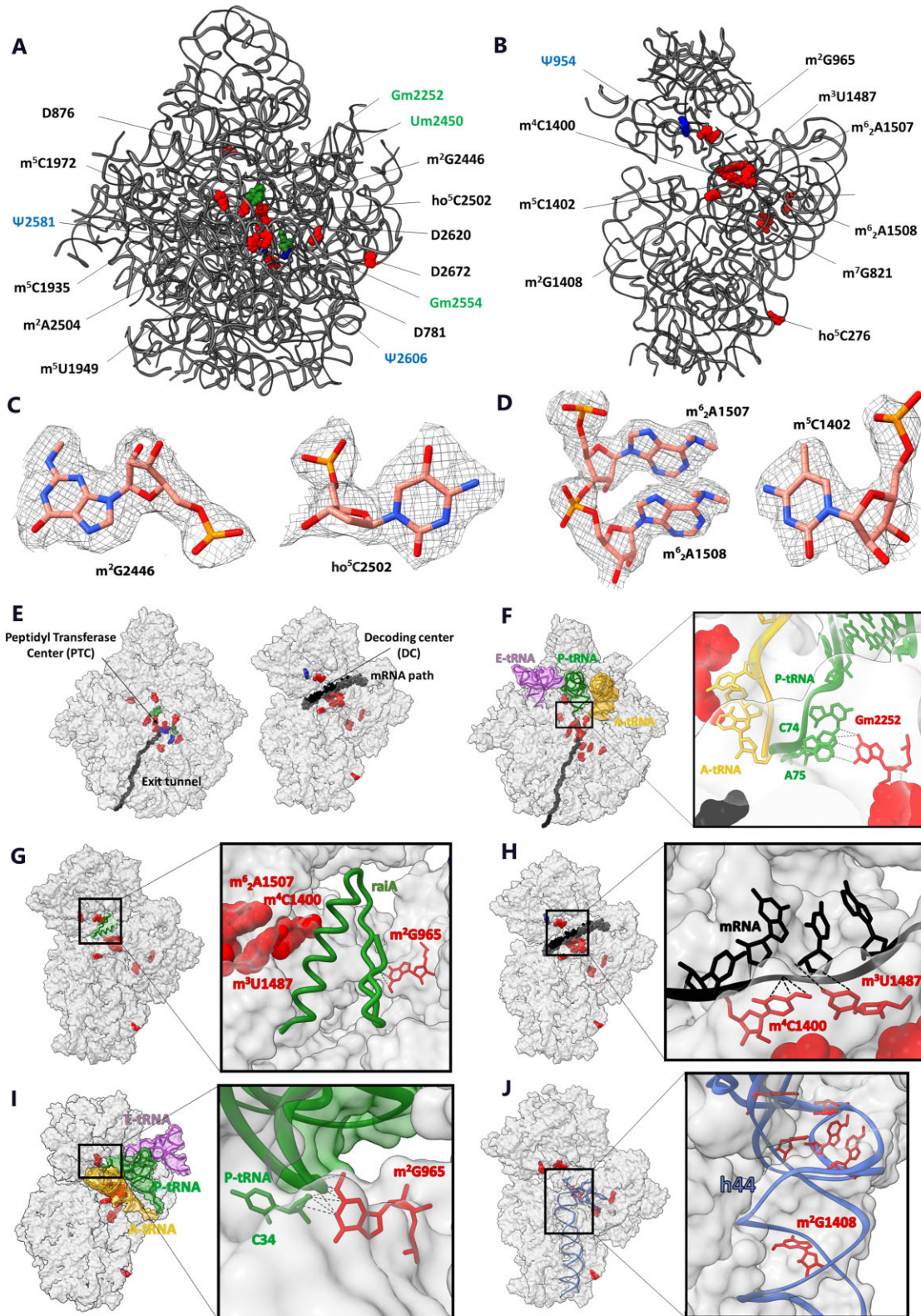
Figure 6. rRNA modifications modeled in the PG ribosome structure (**A**) LSU and (**B**) SSU rRNA base modifications are shown in red, sugar modifications in green, and Ψ modifications are shown in blue. (**C**) LSU examples of rRNA modifications as modeled in PG ribosome cryo-EM map. The map contour level is 1.9σ. (**D**) SSU examples of rRNA modifications modeled within the cryo-EM map. The map contour level is 1.9σ. (**E**) LSU rRNA modifications have been modeled mostly within the PTC and around the protein exit tunnel, whereas the SSU modifications are mostly with the DC and mRNA path. (**F**) Specific rRNA modification interactions in LSU with P-tRNA. Specific rRNA modification interactions in SSU; (**G**) interaction of m^{2}G965 with raiA; (**H**) interaction of m^{4}C1400 and m^{3}U1487 with mRNA; (**I**) interaction of m^{2}G965 with P-tRNA; and (**J**) rRNA modifications in h44.

Table 2. RNA modifications in PG ribosome

rRNA	Modified nucleotide number	EC nucleotide number	Nucleotide	Type	LC/MS	PG70SW83	PG70S-ermΔporN	PG50S-ermΔporN-lef
23S	781	746	U	D	✓	✓	✓	✓
	876	842	U	D	✓	✓	✓	✓
	1921	1911	U	Ψ	✓			
	1925	1915	U	Ψ	✓			
	1927	1917	U	Ψ	✓			
	1935	1925	C	m^5C	✓		✓	✓
	1949	1943	U	m^5U	✓	✓	✓	✓
	1972	1966	C	m^5C	✓	✓	✓	✓
	2067	2057	A	m^6A	✓		✓	✓
	2068	2058	A	m^6_2A	✓		✓	✓
	2069	2059	A	m^6A	✓		✓	✓
	2070	2060	A	m^6A	✓			
	2252	2251	G	Gm	✓	✓	✓	✓
	2446	2445	G	m^2G	✓	✓	✓	✓
	2450	2449	U	Um	✓	✓	✓	✓
	2502	2505	C	ho^5C	✓	✓	✓	✓
	2504	2507	A	m^2A	✓	✓	✓	✓
	2554	2557	G	Gm	✓			✓
	2581	2584	U	Ψ	✓	✓	✓	✓
	2606	2609	U	Ψ	✓	✓	✓	✓
	2620	2619	U	D	✓	✓	✓	✓
	2672	2672	U	D	✓			✓
16S	276	271	C	ho^5C	✓	✓	✓	
	527	527	G	*	✓			
	531	531	U	*	✓			
	821	821	G	m^7G	✓	✓	✓	
	851	851	G	*	✓			
	954	955	U	Ψ	✓		✓	
	965	966	G	m^2G	✓		✓	
	1400	1402	C	m^4C	✓	✓	✓	
	1402	1404	C	m^5C	✓	✓	✓	
	1408	1410	G	m^2G	✓	✓	✓	
	1487	1498	U	m^3U	✓	✓	✓	
	1507	1518	A	m^6_2A	✓	✓	✓	
	1508	1519	A	m^6_2A	✓	✓	✓	

Gm, $O2'$-methylguanosine-$5'$-monophosphate; **Um,** $O2'$-methyluridine-$5'$-monophosphate; **m^5C,** 5-methylcytidine-$5'$-monophosphate; **Ψ,** pseudouridine; **D,** dihydrouridine; **m^7G,** 7-methylguanosine-$5'$-monophosphate; **m^5U,** 5-methyluridine-$5'$-monophosphate; **m^6A,** N6-methyldeoxyadenosine-$5'$-monophoshate; **ho^5C,** 5-hydroxycytidine-$5'$-monophosphate; **m^2A,** 2-methyladenosine-$5'$-monophosphate; **m^6_2A,** N6-dimethyladenosine-$5'$-monophoshate; **m^2G,** 2-methylguanosine-$5'$-monophosphate; **m^4C,** N4,$O2'$-methylcytidine-$5'$-monophosphate; **m^3U,** 3-methyluridine-$5'$-monophosphate; and * nucleotide identified as modified by LC–MS, but the specific modification could not be confidently modeled in the EM map.

(Fig. 8D) and SA (Fig. 8E) ribosomes and their superposition illustrate the high structural similarity of drug binding in these species (Fig. 8F and G).

As previously shown in all structures of complexes of known bacterial ribosomes that interact with pleuromutilin, nucleotides A2062, U2585, and U2504 constitute the pleuromutilin binding pockets. In contrast, their counterparts in eukaryotic ribosomes possess the same sequence identities but adopt different orientations, which prevent such interactions (Supplementary Fig. S10). As previously described, in archaeal and eukaryotic ribosomes, nucleotide U2504 forms a pi-stacking interaction with A2055 that points away from the PTC binding site (Supplementary Fig. S10). This interaction pushes U2504 out of the binding pocket, leaving it open for impeding pleuromutilin binding. This distinction in orientation confers selectivity, distinguishing between bacterial and eukaryotic ribosomes in terms of the pleuromutilin binding.

In parallel, we tested the susceptibility of PG isolates to lefamulin and other antibiotics. The antimicrobial activity of lefamulin, clindamycin, meropenem, metronidazole, tigecycline, and vancomycin was evaluated against a set of clinical *Porphyromonas* spp. isolates (Table 3). All isolates were inhibited by lefamulin at an MIC of 0.03 µg/ml ($MIC_{50/90}$ of 0.03/0.03) and by clindamycin, meropenem, and metronidazole at MICs of $\leq$ 0.03–0.06 µg/ml ($MIC_{50/90}$ of $\leq$ 0.03/0.06), while the activity of vancomycin appeared to be limited against the single tested isolate (MIC of 8 µg/ml).

Discussion

In this study, we present the near-atomic structures of the ribosome from the human pathogen PG, namely PG70SW83 and its isogenic mutant PG70S-ermΔporN, the first being virulent and the latter a macrolide-resistant benign mutant strain. Examining these structures, we deciphered the species-specific features of PG ribosomes. These include a shorter loop D in 5S rRNA that disrupts its interactions with ribosomal components H39 and uL16, resulting in a "hole" in PG ribosome compared to the ribosomes of other organisms. However, we were unable to model four nucleotide residues of the 5S rRNA belonging to loop D due to poor density in PG70SW83, PG70S-ermΔporN, and PG50S-ermΔporN-lef.
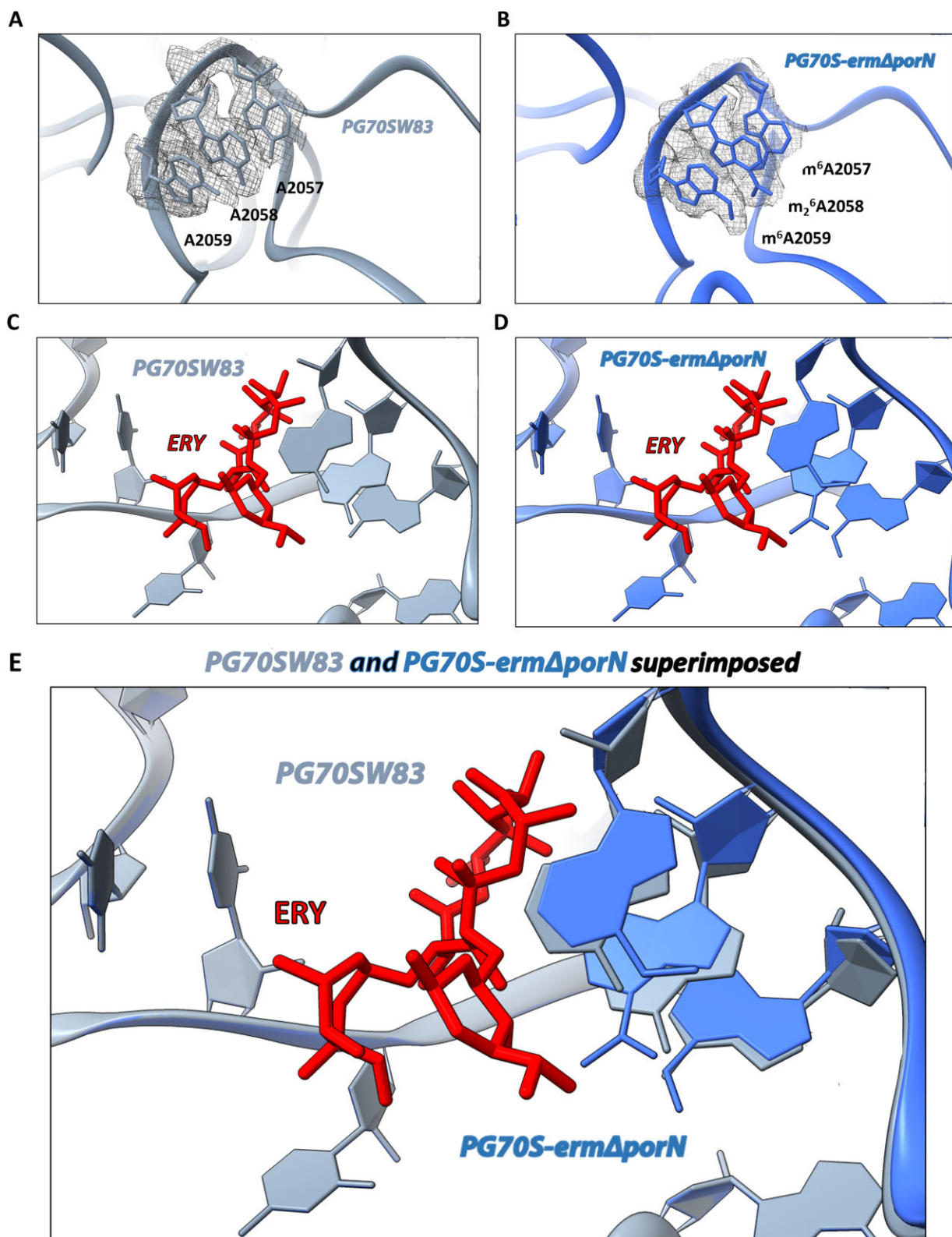
Figure 7. Macrolide resistance due to the rRNA modifications specific to ΔporN strain located at the macrolides binding site. rRNA nucleotides of the macrolide binding pocket (**A**) in PG70SW83 and (**B**) in PG70S-ermΔporN as modeled in the cryo-EM map. Panels (**C**) and (**D**) illustrate the docking of erythromycin (from PDBID 6ND6 [48]) on both PG70SW83 and PG70S-ermΔporN structures. (**E**) Superimposition of both structures is shown in panels (C) and (D).
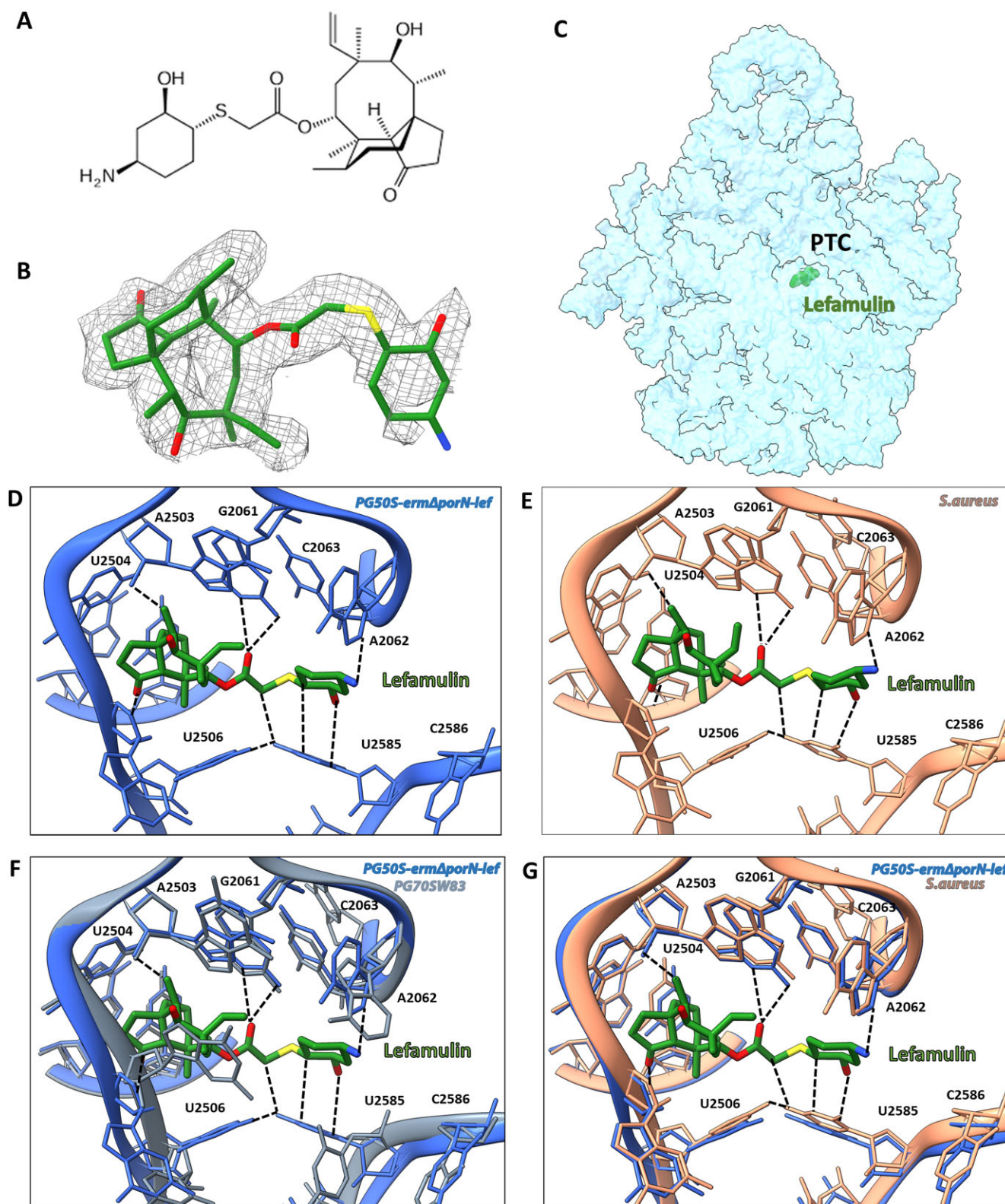
Figure 8. (**A**) The chemical structure of lefamulin. (**B**) Lefamulin modeled within the cryo-EM map of PG50S-ermΔporN-lef. The map contour level is 1.5σ. (**C**) The binding site of lefamulin (green) within the PG50S-ermΔporN-lef complex structure at the PTC. (**D–G**) Comparison between the binding pocket of PG50S-ermΔporN-lef complex (shown in blue), PG70SW83 (shown in gray), and SA70S-lef complex (PDB ID 5HL7, shown in salmon).

Porphyromonas spp. ($N = 10$)[a]	MIC_{50} (µg/ml)	MIC_{90} (µg/ml)	Range (µg/ml)
Lefamulin	0.03	0.03	0.03–0.03
Clindamycin	≤0.03	0.06	≤0.03–0.06
Meropenem	≤0.03	0.06	≤0.03–0.06
Metronidazole	≤0.03	0.06	≤0.03–0.06
Tigecycline[b]	–	–	0.06
Vancomycin[b]	–	–	8

[a]Includes PG ATCC33277, clinical PG isolates ($N = 8$), and unspeciated *Porphyromonas* spp. ($N = 1$).
[b]MIC tested only against PG ATCC33277.

The poor density at the 5S rRNA tip of PG ribosome suggests that the shorter D-loop is dynamic. A similar shorter loop D was observed in *M. smegmatis* ribosome [67]. However, the novel *M. smegmatis* rProtein bL37, belonging to the mycobacterium family, is bound near its 5S rRNA loop D, thus stabilizing the loop D tip. As no similar feature was identified in the PG genome and structure, this cavity could allow for species-specific interactions required for PG protein translation, which maintains its functionality despite this structural void. As 5S rRNA acts as an adapter of different functional sites of the ribosome, this "hole" may also provide a potential drug target for PG ribosome.

Additionally, we were able to model bS22, located near the DC of the ribosome, which interacts with h44 and h45 of SSU, and H70 of LSU, forming an additional intersubunit bridge element and stabilizing PG70S ribosome. Its discovery in *M. smegmatis* 70S ribosomes unveils a previously unknown player absent in EC ribosomes [67]. Notably, bS22 is structurally similar to the C-terminus of mitochondrial rProtein mS38 and eukaryotic cytosolic rProtein eL41. This similarity tempts us to speculate a case of convergent evolution, wherein distinct organisms independently develop analogous traits or features.

Rich in arginines and lysines, bS22 appears to play a crucial role through its interactions with helices in the both 23S and 16S rRNA. For instance, it may help stabilize h44, which undergoes significant conformational changes during tRNA translocation [69]. Furthermore, its proposed interaction with H45 near the mRNA exit site implies a regulatory function in modulating the mRNA channel's architecture. This interaction potentially influences leaderless translation initiation, a prevalent mechanism in mycobacteria [107], mitochondria [108], and Bacteroidetes [75], where a significant portion of the transcriptome lacks SD sequences. The disruption of the interaction between bS22 and mS38 with the h44 of SSU has been demonstrated to enhance the sensitivity of aminoglycoside antibiotics in both *M. smegmatis* [71] and *Saccharomyces cerevisiae* [109]. This strategy may demonstrate potential in combating aminoglycoside-resistant strains of PG. Targeting this interaction may be a feasible mechanism to restore sensitivity to aminoglycosides in PG, offering a potential therapeutic strategy against this pathogen and its resistant strains, although additional research is required to elucidate the mechanisms underlying this mode of inhibition.

Furthermore, our study highlights structural differences in specific rProteins within the PG ribosome. Notably, uS4 features a shorter loop, leading to the loss of interactions with

16S rRNA. The extended C-terminus of bS16 in PG that reaches the platform and uS4 is absent in other ribosomes and creates a unique interaction with 16S rRNA, thus stabilizing the 30S subunit. Hence, by disrupting crucial ribosomal interactions, the structural distinctions among rProteins offer promising avenues for developing novel drugs specific against PG.

Additionally, our findings demonstrate that *RPL38* is essential for the survival of PG, as its deletion was only possible when a plasmid-expressed copy was provided. This highlights the critical role of bL38 in ribosome function. To gain further insights into its structural dynamics, we performed MD simulations, which revealed that bL38 maintains a predominantly β-strand architecture with stable core elements and flexible loop and terminal regions. The observed structural fluctuations, particularly at the N- and C-termini, suggest a degree of conformational adaptability. This dynamic behavior may facilitate interactions with ribosomal components or contribute to the protein's functional role within the PG ribosome, potentially influencing ribosome assembly or translation regulation.

Our study further explores rRNA modifications in PG ribosomes, and highlights their importance in ribosome integrity and function. Notably, the PG ribosome appears to be highly modified compared to other bacterial ribosomes, though the underlying reasons for this extensive modification remain unclear. To our knowledge, this is the first study to identify and confirm rRNA modifications in the Bacteroidetes ribosome, including the unique m^2G1408 modification near the aminoglycoside binding site. This species-specific modification, absent in other bacterial ribosomes, presents a promising target for antibiotic development, offering opportunities for designing aminoglycoside derivatives that selectively bind to Bacteroidetes ribosomes. Additionally, the strategic positioning of these modifications, especially around the PTC and DC, suggests their involvement in critical specific ribosomal activities. The potential role of rRNA modifications in stress and stationary phase responses underscores their significance in PG adaptation to environmental challenges.

We also provide insights into macrolide resistance mechanisms in PG by identifying distinctive rRNA modifications in the ermΔporN strain, where the PG_0266 gene has been substituted with the *erm* cassette, which encodes an adenosine methyltransferase—confers resistance to macrolides, lincosamides, and streptogramin B [31, 32]. However, in PG ribosome, four methylated adenosines were detected by mass spectrometry, and three were detected in the EM map, an unusual finding for an adenosine methyltransferase enzyme. This expanded repertoire of modifications highlights the unique biochemical and structural properties of the PG ribosome. These rRNA modifications that may hinder the binding of macrolide antibiotics shed light on this resistance mechanism, suggesting potential strategies to overcome them.

Notably, our study also suggests the prospective repurposing of lefamulin, a pleuromutilin derivative, currently in clinical use against *S. pneumoniae*, *S. aureus*, *Haemophilus influenzae*, *Moraxella catarrhalis*, *Legionella pneumophila*, *C. pneumoniae,* and *M. pneumoniae*, as a promising antibiotic option for combating resistant strains of PG, particularly, the notable resistance observed towards macrolides. Thus, lefamulin demonstrates potent antimicrobial activity at an MIC value of 0.03 µg/ml against clinical PG isolates by utilizing a distinct binding mode compared to macrolides. The cryo-EM

structure PG50S-ermΔ*porN*-lef elucidates the mechanism by which lefamulin impedes the ribosomal A- and P-sites and disrupts tRNA accommodation, in accordance with prior observations in other ribosome–pleuromutilin complex structures. Furthermore, other pleuromutilins as well as other antibiotics that remain unaffected by adenosine methylation offer promising approaches for tackling macrolide-resistant strains of PG.

In summary, our study of the structure of the PG ribosomes provides a detailed understanding of their structural and functional attributes, highlighting distinctive features that set them apart from other bacterial ribosomes. These distinctions present potential targets for drug development, particularly in combating periodontal disease and understanding antibiotic resistance mechanisms. Moreover, the study underscores the significance of rRNA modifications in PG ribosome functional centers and their potential roles in stress responses, thereby expanding our insights into the adaptive strategies employed by PG. In conclusion, this research opens new avenues for future investigations and therapeutic interventions aimed at systemic treatments of PG-related infections.

Acknowledgements

Supplementary data

Supplementary data is available at NAR online.

Conflict of interest

S.P. was a former employee of Nabriva Therapeutics. The other authors declare no competing interests.

Funding

Data availability

The cryo-EM density maps of the PG ribosome have been deposited in the Electron Microscopy Data Bank (EMDB) under accession numbers EMD-52641 (PG70SW83), EMD-52640 (PG70S-ermΔporN), and EMD-52635 (PG50S-ermΔporN-lef). Atomic coordinates and structure factors have been deposited in the Protein Data Bank (PDB) under accession codes 9I5X (PG70SW83), 9I5V (PG70S-ermΔporN), and 9I5T (PG50S-ermΔporN-lef). The RNA LC–MS data have been deposited to the ProteomeXchange Consortium via the jPOST partner repository (https://repository.jpostdb.org/) with the dataset identifier PXD054164 (JPST003226).

References

1. Poehlsgaard J, Douthwaite S. The bacterial ribosome as a target for antibiotics. *Nat Rev Microbiol* 2005;**3**:870–81. https://doi.org/10.1038/nrmicro1265
2. Auerbach T, Bashan A, Harms J *et al.* Antibiotics targeting ribosomes: crystallographic studies. *Curr Drug Targets Infect Disord* 2002;**2**:169–86. https://doi.org/10.2174/1568005023342506
3. Wilson DN, Beckmann R. The ribosomal tunnel as a functional environment for nascent polypeptide folding and translational stalling. *Curr Opin Struct Biol* 2011;**21**:274–82. https://doi.org/10.1016/j.sbi.2011.01.007
4. Eyal Z, Matzov D, Krupkin M *et al.* Structural insights into species-specific features of the ribosome from the pathogen *Staphylococcusaureus*. *Proc Natl Acad Sci USA* 2015;**112**:E5805–14.
5. Halfon Y, Jimenez-Fernandez A, Rosa RL *et al.* Structure of *Pseudomonasaeruginosa* ribosomes from an aminoglycoside-resistant clinical isolate. *Proc Natl Acad Sci USA* 2019;**116**:22275–81. https://doi.org/10.1073/pnas.1909831116
6. Shalev-Benami M, Zhang Y, Matzov D *et al.* 2.8-Å cryo-EM structure of the large ribosomal subunit from the eukaryotic parasite *leishmania*. *Cell Rep* 2016;**16**:288–94. https://doi.org/10.1016/j.celrep.2016.06.014
7. Hiregange DG, Rivalta A, Bose T *et al.* Cryo-EM structure of the ancient eukaryotic ribosome from the human parasite *Giardialamblia*. *Nucleic Acids Res* 2022;**50**:1770–82. https://doi.org/10.1093/nar/gkac046
8. Helena-Bueno K, Kopetschke S, Filbeck S *et al.* Structurally heterogeneous ribosomes cooperate in protein synthesis in bacterial cells. *Nat Commun* 2025;**16**:2751. https://doi.org/10.1038/s41467-025-57955-8
9. Cimicata G, Bose T, Fridkin G *et al.* Contemporary challenges in medical usage of antibiotics. The Pontifical Academy of Sciences, 2020.
10. Cimicata G, Fridkin G, Bose T *et al.* Structural studies reveal the role of helix 68 in the elongation step of protein biosynthesis. *mBio* 2022;**13**:e0030622. https://doi.org/10.1128/mbio.00306-22
11. Wingrove JA, DiScipio RG, Chen Z *et al.* Activation of complement components C3 and C5 by a cysteine proteinase (gingipain-1) from *Porphyromonas* (Bacteroides) *gingivalis*. *J Biol Chem* 1992;**267**:18902–7. https://doi.org/10.1016/S0021-9258(19)37046-2
12. Curtis MA, Thickett A, Slaney JM *et al.* Variable carbohydrate modifications to the catalytic chains of the RgpA and RgpB proteases of *Porphyromonas gingivalis* W50. *Infect Immun* 1999;**67**:3816–23. https://doi.org/10.1128/IAI.67.8.3816-3823.1999
13. Potempa J, Banbula A, Travis J. Role of bacterial proteinases in matrix destruction and modulation of host responses. *Periodontology 2000* 2000;**24**:153–92. https://doi.org/10.1034/j.1600-0757.2000.2240108.x

14. Mougeot JC, Stevens CB, Paster BJ *et al*. *Porphyromonas gingivalis* is the most abundant species detected in coronary and femoral arteries. *J Oral Microbiol* 2017;**9**:1281562. https://doi.org/10.1080/20002297.2017.1281562

15. Sohn J, Li L, Zhang L *et al*. *Porphyromonas gingivalis* indirectly elicits intestinal inflammation by altering the gut microbiota and disrupting epithelial barrier function through IL9-producing CD4$^+$ T cells. *MolOral Microbiol* 2022;**37**:42–52. https://doi.org/10.1111/omi.12359

16. Wang X, Jia Y, Wen L *et al*. *Porphyromonas gingivalis* promotes colorectal carcinoma by activating the hematopoietic NLRP3 inflammasome. *Cancer Res* 2021;**81**:2745–59. https://doi.org/10.1158/0008-5472.CAN-20-3827

17. Chen Y, Zhou R, Yi Z *et al*. *Porphyromonas gingivalis* induced inflammatory responses and promoted apoptosis in lung epithelial cells infected with H1N1 via the bcl-2/Bax/caspase-3 signaling pathway. *Mol Med Rep* 2018;**18**:97–104.

18. Kanagasingam S, Chukkapalli SS, Welbury R *et al*. *Porphyromonas gingivalis* is a strong risk factor for Alzheimer's disease. *J Alzheimers Dis Rep* 2020;**4**:501–11. https://doi.org/10.3233/ADR-200250

19. Dominy SS, Lynch C, Ermini F *et al*. *Porphyromonas gingivalis* in Alzheimer's disease brains: evidence for disease causation and treatment with small-molecule inhibitors. *Sci Adv* 2019;**5**:eaau3333. https://doi.org/10.1126/sciadv.aau3333

20. Sao P, Vats S, Singh S. *Porphyromonas gingivalis* resistance and virulence: an integrated functional network analysis. *Gene* 2022;**839**:146734. https://doi.org/10.1016/j.gene.2022.146734

21. Conrads G, Klomp T, Deng D *et al*. The antimicrobial susceptibility of *Porphyromonas gingivalis*: genetic repertoire, global phenotype, and review of the literature. *Antibiotics* 2021;**10**:1438. 10.3390/antibiotics10121438

22. Rams TE, Sautter JD, van Winkelhoff AJ. Comparative *in vitro* resistance of human periodontal bacterial pathogens to tinidazole and four other antibiotics. *Antibiotics* 2020;**9**:68. https://doi.org/10.3390/antibiotics9020068

23. Rams TE, Sautter JD, van Winkelhoff AJ. Emergence of antibiotic-resistant *Porphyromonas gingivalis* in United States periodontitis patients. *Antibiotics (Basel)* 2023;**12**:1584.

24. Gerits E, Verstraeten N, Michiels J. New approaches to combat *Porphyromonas gingivalis* biofilms. *JOral Microbiol* 2017;**9**:1300366. https://doi.org/10.1080/20002297.2017.1300366

25. Cook GS, Costerton JW, Lamont RJ. Biofilm formation by *Porphyromonas gingivalis* and *Streptococcus gordonii*. *J Periodontal Res* 1998;**33**:323–7. https://doi.org/10.1111/j.1600-0765.1998.tb02326.x

26. Kapoor A, Malhotra R Fau - Grover V, Grover V Fau - Grover D *et al*. Systemic antibiotic therapy in periodontics. *Dent Res J* 2012;**9**:505–15. https://doi.org/10.4103/1735-3327.104866

27. Keestra JA, Grosjean I, Coucke W *et al*. Non-surgical periodontal therapy with systemic antibiotics in patients with untreated aggressive periodontitis: a systematic review and meta-analysis. *J Periodontal Res* 2015;**50**:689–706. https://doi.org/10.1111/jre.12252

28. Howard KC, Gonzalez OA, Garneau-Tsodikova S. *Porphyromonas gingivalis*: where do we stand in our battle against this oral pathogen? *RSC Med Chem* 2021;**12**:666–704. https://doi.org/10.1039/D0MD00424C

29. Jha V, Roy B, Jahagirdar D *et al*. Structural basis of sequestration of the anti-Shine–Dalgarno sequence in the Bacteroidetes ribosome. *Nucleic Acids Res* 2021;**49**:547–67. https://doi.org/10.1093/nar/gkaa1195

30. Benedyk MA-O, Marczyk A, Chruścicka B. Type IX secretion system is pivotal for expression of gingipain-associated virulence of *Porphyromonas gingivalis*. *Mol Oral Microbiol* 2019;**34**:237–44. https://doi.org/10.1111/omi.12268

31. Svetlov MS, Syroegin EA, Aleksandrova EV *et al*. Structure of Erm-modified 70S ribosome reveals the mechanism of macrolide resistance. *Nat Chem Biol* 2021;**17**:412–20. https://doi.org/10.1038/s41589-020-00715-0

32. Weisblum B. Erythromycin resistance by ribosome modification. *Antimicrob Agents Chemother* 1995;**39**:577–85. https://doi.org/10.1128/AAC.39.3.577

33. Eyal Z, Matzov D, Krupkin M *et al*. A novel pleuromutilin antibacterial compound, its binding mode and selectivity mechanism. *Sci Rep* 2016;**6**:39004. https://doi.org/10.1038/srep39004

34. Lee YA-O, Jacobs KL. Leave it to lefamulin: a pleuromutilin treatment option in community-acquired bacterial pneumonia. *Drugs* 2019;**79**:1867–76, https://doi.org/10.1007/s40265-019-01219-5

35. Lasica AM, Goulas T, Mizgalska D *et al*. Structural and functional probing of PorZ, an essential bacterial surface component of the type-IX secretion system of human oral-microbiomic *Porphyromonas gingivalis*. *Sci Rep* 2016;**6**:37708. https://doi.org/10.1038/srep37708

36. Fletcher HM, Schenkein HA, Morgan RM *et al*. Virulence of a *Porphyromonas gingivalis* W83 mutant defective in the prtH gene. *Infect Immun* 1995;**63**:1521–8. https://doi.org/10.1128/iai.63.4.1521-1528.1995

37. Zivanov J, Nakane T, Forsberg BO *et al*. New tools for automated high-resolution cryo-EM structure determination in RELION-3. *eLife* 2018;**7**:e42166. https://doi.org/10.7554/eLife.42166

38. Scheres SHW. A bayesian view on cryo-EM structure determination. *J Mol Biol* 2012;**415**:406–18. https://doi.org/10.1016/j.jmb.2011.11.010

39. Zheng SQ, Palovcak E, Armache J-P *et al*. MotionCor2: anisotropic correction of beam-induced motion for improved cryo-electron microscopy. *Nat Methods* 2017;**14**:331–2. https://doi.org/10.1038/nmeth.4193

40. Mindell JA, Grigorieff N. Accurate determination of local defocus and specimen tilt in electron microscopy. *J Struct Biol* 2003;**142**:334–47. https://doi.org/10.1016/S1047-8477(03)00069-8

41. Scheres SHW. Amyloid structure determination in RELION-3.1. *Acta Crystallogr D Struct Biol* 2020;**76**:94–101. https://doi.org/10.1107/S2059798319016577

42. Nakane T, Kimanius D, Lindahl E *et al*. Characterisation of molecular motions in cryo-EM single-particle data by multi-body refinement in RELION. *eLife* 2018;**7**:e36861. https://doi.org/10.7554/eLife.36861

43. Kucukelbir A, Sigworth FJ, Tagare HD. Quantifying the local resolution of cryo-EM density maps. *Nat Methods* 2014;**11**:63–5. https://doi.org/10.1038/nmeth.2727

44. Emsley P, Lohkamp B, Scott WG *et al*. Features and development of Coot. *Acta Crystallogr D Biol Crystallogr* 2010;**66**:486–501. https://doi.org/10.1107/S0907444910007493

45. Breiner-Goldstein E, Eyal Z, Matzov D *et al*. Ribosome-binding and anti-microbial studies of the mycinamicins, 16-membered macrolide antibiotics from *Micromonospora griseorubida*. *Nucleic Acids Res* 2021;**49**:9560–73. https://doi.org/10.1093/nar/gkab684

46. Gagnon MG, Lin J, Bulkley D *et al*. Crystal structure of elongation factor 4 bound to a clockwise ratcheted ribosome. *Science* 2014;**345**:684–7. https://doi.org/10.1126/science.1253525

47. Waterhouse A, Bertoni M, Bienert S *et al*. SWISS-MODEL: homology modelling of protein structures and complexes. *Nucleic Acids Res* 2018;**46**:W296–303. https://doi.org/10.1093/nar/gky427

48. Pettersen EF, Goddard TD, Huang CC *et al*. UCSF Chimera—a visualization system for exploratory research and analysis. *J Comput Chem* 2004;**25**:1605–12. https://doi.org/10.1002/jcc.20084

49. Goddard TD, Huang CC, Meng EC *et al*. UCSF ChimeraX: meeting modern challenges in visualization and analysis. *Protein Sci* 2018;**27**:14–25. https://doi.org/10.1002/pro.3235

50. Pettersen EF, Goddard TD, Huang CC *et al*. UCSF ChimeraX: structure visualization for researchers, educators, and developers. *Protein Sci* 2021;**30**:70–82. https://doi.org/10.1002/pro.3943

51. Afonine PV, Poon BK, Read RJ *et al*. Real-space refinement in PHENIX for cryo-EM and crystallography. *Acta Crystallogr D Struct Biol* 2018;**74**:531–44. https://doi.org/10.1107/S2059798318006551

52. Williams CJ, Headd JJ, Moriarty NW *et al*. MolProbity: more and better reference data for improved all-atom structure validation. *Protein Sci* 2018;**27**:293–315. https://doi.org/10.1002/pro.3330

53. Waterhouse AM, Procter JB, Martin DMA *et al*. Jalview Version 2—a multiple sequence alignment editor and analysis workbench. *Bioinformatics* 2009;**25**:1189–91, https://doi.org/10.1093/bioinformatics/btp033

54. Szczęśniak K, Veillard F, Scavenius C *et al*. The bacteroidetes Q-rule and glutaminyl cyclase activity increase the stability of extracytoplasmic proteins. *mBio* 2023;**14**:e0098023, https://doi.org/10.1128/mbio.00980-23

55. Bowers KJ, Chow E, Xu H *et al*. Scalable algorithms for molecular dynamics simulations on commodity clusters. In: *SC '06: Proceedings of the 2006 ACM/IEEE Conference on Supercomputing*. 2006, 84.

56. Abramson J, Adler J, Dunger J *et al*. Accurate structure prediction of biomolecular interactions with AlphaFold 3. *Nature* 2024;**630**:493–500, https://doi.org/10.1038/s41586-024-07487-w

57. Yamauchi Y, Taoka M, Nobe Y *et al*. Denaturing reversed phase liquid chromatographic separation of non-coding ribonucleic acids on macro-porous polystyrene-divinylbenzene resins. *J Chromatogr A* 2013;**1312**:87–92. https://doi.org/10.1016/j.chroma.2013.09.021

58. Taoka M, Nobe Y, Hori M *et al*. A mass spectrometry-based method for comprehensive quantitative determination of post-transcriptional RNA modifications: the complete chemical structure of S*chizosaccharomyces pombe* ribosomal RNAs. *Nucleic Acids Res* 2015;**43**:e115. https://doi.org/10.1093/nar/gkv560

59. Nakayama H, Yamauchi Y, Taoka M *et al*. Direct identification of human cellular microRNAs by nanoflow liquid chromatography–high-resolution tandem mass spectrometry and database searching. *Anal Chem* 2015;**87**:2884–91. https://doi.org/10.1021/ac504378s

60. Nakayama H, Nobe Y, Koike M *et al*. Liquid chromatography–mass spectrometry-based qualitative profiling of mRNA therapeutic reagents using stable isotope-labeled standards followed by the automatic quantitation software Ariadne. *Anal Chem* 2023;**95**:1366–75.

61. Nakayama H, Akiyama M, Taoka M *et al*. Ariadne: a database search engine for identification and chemical analysis of RNA using tandem mass spectrometry data. *Nucleic Acids Res* 2009;**37**:e47. https://doi.org/10.1093/nar/gkp099

62. CarpenterDE. *Methods for Antimicrobial Susceptibility Testing of Anaerobic Bacteria*. 9th edn., Pittsburgh, PA, clinical laboratory standards institute, 2018.

63. Petrov AS, Bernier CR, Hershkovits E *et al*. Secondary structure and domain architecture of the 23S and 5S rRNAs. *Nucleic Acids Res* 2013;**41**:7522–35. https://doi.org/10.1093/nar/gkt513

64. Szymanski M, Zielezinski A, Barciszewski J *et al*. 5SRNAdb: an information resource for 5S ribosomal RNAs. *Nucleic Acids Res* 2016;**44**:D180–3. https://doi.org/10.1093/nar/gkv1081

65. Sergiev PV, Bogdanov A, Fau - Dahlberg AE *et al*. Mutations at position A960 of *E. coli* 23S ribosomal RNA influence the structure of 5S ribosomal RNA and the peptidyltransferase region of 23S ribosomal RNA. *J Mol Biol* 2000;**299**:379–89. https://doi.org/10.1006/jmbi.2000.3739

66. Hentschel J, Burnside C, Mignot I *et al*. The complete structure of the *Mycobacterium smegmatis* 70S ribosome. *Cell Rep* 2017;**20**:149–60. https://doi.org/10.1016/j.celrep.2017.06.029

67. Li Z, Ge X, Zhang Y *et al*. Cryo-EM structure of *Mycobacterium smegmatis* ribosome reveals two unidentified ribosomal proteins close to the functional centers. *Protein Cell* 2018;**9**:384–8.

68. Khatter H, Myasnikov AG, Natchiar SK *et al*. Structure of the human 80S ribosome. *Nature* 2015;**520**:640–5, https://doi.org/10.1038/nature14427

69. VanLoock MS, Agrawal RK, Gabashvili IS *et al*. Movement of the decoding region of the 16S ribosomal RNA accompanies tRNA translocation. *J Mol Biol* 2000;**304**:507–15. https://doi.org/10.1006/jmbi.2000.4213

70. Mishra S, Ahmed T, Tyagi A *et al*. Structures of *Mycobacterium smegmatis* 70S ribosomes in complex with HPF, tmRNA, and P-tRNA. *Sci Rep* 2018;**8**:13587. https://doi.org/10.1038/s41598-018-31850-3

71. Majumdar S, Deep A, Sharma MR *et al*. The small mycobacterial ribosomal protein, bS22, modulates aminoglycoside accessibility to its 16S rRNA helix-44 binding site. bioRxiv, http://doi.org/10.1101/2023.03.31.535098, 1 April 2023, preprint: not peer reviewed.

72. Abeysirigunawardena SC, Kim HA-O, Lai J *et al*. Evolution of protein-coupled RNA dynamics during hierarchical assembly of ribosomal complexes. *Nat Commun* 2017;**8**:492. https://doi.org/10.1038/s41467-017-00536-1

73. Matzov D, Aibara S, Basu A *et al*. The cryo-EM structure of hibernating 100S ribosome dimer from pathogenic *Staphylococcus aureus*. *Nat Commun* 2017;**8**:723. https://doi.org/10.1038/s41467-017-00753-8

74. Nakagawa S, Niimura Y Fau - Miura K-i, Miura K Fau - Gojobori T *et al*. Dynamic evolution of translation initiation mechanisms in prokaryotes. *Proc Natl Acad Sci USA* 2010;**107**:6382–7. https://doi.org/10.1073/pnas.1002036107

75. Nakagawa S, Niimura Y, Gojobori T. Comparative genomic analysis of translation initiation mechanisms for genes lacking the Shine–Dalgarno sequence in prokaryotes. *Nucleic Acids Res* 2017;**45**:3922–31. https://doi.org/10.1093/nar/gkx124

76. Wegmann U, Horn N, Carding SR. Defining the bacteroides ribosomal binding site. *Appl Environ Microb* 2013;**79**:1980–9. https://doi.org/10.1128/AEM.03086-12

77. Accetto T, Avguštin G. Inability of *Prevotella bryantii* to form a functional Shine–Dalgarno interaction reflects unique evolution of ribosome binding sites in Bacteroidetes. *PLoS One* 2011;**6**:e22914. https://doi.org/10.1371/journal.pone.0022914

78. Lim K, Furuta Y, Fau - Kobayashi I *et al*. Large variations in bacterial ribosomal RNA genes. *Mol Biol Evol* 2012;**229**:2937–48. https://doi.org/10.1093/molbev/mss101

79. Amin MR, Yurovsky A, Chen YA-O *et al*. Re-annotation of 12,495 prokaryotic 16S rRNA 3′ ends and analysis of Shine–Dalgarno and anti-Shine–Dalgarno sequences. *PLoS One* 2018;**13**:e0202767. https://doi.org/10.1371/journal.pone.0202767

80. Green R, Noller HF. *In vitro* complementation analysis localizes 23S rRNA posttranscriptional modifications that are required for *Escherichiacoli* 50S ribosomal subunit assembly and function. *RNA* 1996;**2**:1011–21.

81. Watson ZL, Ward FR, Méheust R *et al*. Structure of the bacterial ribosome at 2 Å resolution. *eLife* 2020;**9**:e60482.

82. Fischer N, Neumann P, Konevega AL *et al*. Structure of the *E. coli* ribosome–EF-tu complex at <3 Å resolution by Cs-corrected cryo-EM. *Nature* 2015;**520**:567–70.

83. Popova AM, Jain N, Dong X *et al*. Complete list of canonical post-transcriptional modifications in the *Bacillus subtilis* ribosome and their link to RbgA driven large subunit assembly. *Nucleic Acids Res* 2024; **52**:11203–17. https://doi.org/10.1093/nar/gkae626

84. Polikanov YS, Melnikov SV, Söll D *et al*. Structural insights into the role of rRNA modifications in protein synthesis and ribosome assembly. *Nat Struct Mol Biol* 2015;**22**:11203–17.

85. Lang M, Krin E, Korlowski C *et al*. Sleeping ribosomes: bacterial signaling triggers RaiA mediated persistence to aminoglycosides. *iScience* 2021;**24**:103128. https://doi.org/10.1016/j.isci.2021.103128

86. Maki Y, Yoshida H, Fau - Wada A *et al*. Two proteins, YfiA and YhbH, associated with resting ribosomes in stationary phase *Escherichia coli*. *Genes Cells* 2000;**5**:965–74. https://doi.org/10.1046/j.1365-2443.2000.00389.x

87. Gohara DW, Yap MF. Survival of the drowsiest: the hibernating 100S ribosome in bacterial stress management. *Curr Genet* 2018;**64**:753–60. https://doi.org/10.1007/s00294-017-0796-2

88. Sabharwal D, Song T, Papenfort K *et al*. The VrrA sRNA controls a stationary phase survival factor Vrp of *Vibrio cholerae*. *RNA Biology* 2015;**12**:186–96, https://doi.org/10.1080/15476286.2015.1017211

89. Agafonov DE, Kolb Va Fau - Nazimov IV, Nazimov I *et al*. A protein residing at the subunit interface of the bacterial ribosome. *Proc Natl Acad Sci USA* 1999;**96**:12345–9. https://doi.org/10.1073/pnas.96.22.12345

90. Di Pietro F, Brandi A, Fau - Dzeladini N *et al*. Role of the ribosome-associated protein PY in the cold-shock response of *Escherichia coli*. *MicrobiologyOpen* 2013;**2**:293–307. https://doi.org/10.1002/mbo3.68

91. Agafonov DE, Kolb Va Fau - Spirin AS, Spirin AS. Ribosome-associated protein that inhibits translation at the aminoacyl-tRNA binding stage. *EMBO Rep* 2001;**2**:399–402. https://doi.org/10.1093/embo-reports/kve091

92. Vila-Sanjurjo A, Schuwirth BS, Hau CW *et al*. Structural basis for the control of translation initiation during stress. *Nat Struct Mol Biol* 2004;**11**:1054–9. https://doi.org/10.1038/nsmb850

93. Seistrup KH, Rose S, Birkedal U *et al*. Bypassing rRNA methylation by RsmA/Dim1during ribosome maturation in the hyperthermophilic archaeon *Nanoarchaeumequitans*. *Nucleic Acids Res* 2017;**45**:2007–15.

94. Gorasia DG, Veith PD, Hanssen EG *et al*. Structural insights into the PorK and PorN components of the *Porphyromonas gingivalis* type IX secretion system. *PLoS Pathog* 2016;**12**:e1005820, https://doi.org/10.1371/journal.ppat.1005820

95. Svetlov MA-O, Plessa EA-O, Chen CA-O *et al*. High-resolution crystal structures of ribosome-bound chloramphenicol and erythromycin provide the ultimate basis for their competition. *RNA* 2019;**25**:600–6. https://doi.org/10.1261/rna.069260.118

96. Kavanagh F, Hervey A, Fau - Robbins WJ *et al*. Antibiotic substances from basidiomycetes: VIII. *Pleurotus multilus* (Fr.) Sacc. and *Pleurotus passeckerianus* Pilat. *Proc Natl Acad Sci USA* 1951;**37**:570–4. https://doi.org/10.1073/pnas.37.9.570

97. Hodgin LA, HÖGenauer G. The mode of action of pleuromutilin derivatives. *Eur J Biochem* 1974;**47**:527–33. https://doi.org/10.1111/j.1432-1033.1974.tb03721.x

98. HÖGenauer G. The mode of action of pleuromutilin derivatives. *Eur J Biochem* 1975;**52**:93–8, https://doi.org/10.1111/j.1432-1033.1975.tb03976.x

99. Poulsen SM, Karlsson M, Johansson LB *et al*. The pleuromutilin drugs tiamulin and valnemulin bind to the RNA at the peptidyl transferase centre on the ribosome. *Mol Microbiol* 2001;**41**:1091–9. https://doi.org/10.1046/j.1365-2958.2001.02595.x

100. Paternoga H, Crowe-McAuliffe C, Bock LV *et al*. Structural conservation of antibiotic interaction with ribosomes. *Nat Struct Mol Biol* 2023;**30**:1380–92.

101. Crowe-McAuliffe C, Murina V, Turnbull KJ *et al*. Structural basis of ABCF-mediated resistance to pleuromutilin, lincosamide, and streptogramin A antibiotics in Gram-positive pathogens. *Nat Commun* 2021;**12**:3577, https://doi.org/10.1038/s41467-021-23753-1

102. Long Katherine S, Hansen Lykke H, Jakobsen L *et al*. Interaction of pleuromutilin derivatives with the ribosomal peptidyl transferase center. *Antimicrob Agents Chemother* 2006;**50**:1458–62, https://doi.org/10.1128/AAC.50.4.1458-1462.2006

103. Mp V, Jl W. Lefamulin: review of a promising novel pleuromutilin antibiotic. *Pharmacotherapy* 2018;**38**:935–46.

104. Schlünzen F, Pyetan E, Fucini P *et al*. Inhibition of peptide bond formation by pleuromutilins: the structure of the 50S ribosomal subunit from *Deinococcus radiodurans* in complex with tiamulin. *Mol Microbiol* 2004;**54**:1287–94, https://doi.org/10.1111/j.1365-2958.2004.04346.x

105. Davidovich C, Bashan A, Auerbach-Nevo T *et al*. Induced-fit tightens pleuromutilins binding to ribosomes and remote interactions enable their selectivity. *Proc Natl Acad Sci USA* 2007;**104**:4291–6. https://doi.org/10.1073/pnas.0700041104

106. Gürel G, Blaha G, Moore PB *et al*. U2504 determines the species specificity of the A-site cleft antibiotics:the structures of tiamulin, homoharringtonine, and bruceantin bound to the ribosome. *J Mol Biol* 2009;**389**:146–56. https://doi.org/10.1016/j.jmb.2009.04.005

107. Cortes T, Schubert OT, Rose G *et al*. Genome-wide mapping of transcriptional start sites defines an extensive leaderless transcriptome in *Mycobacterium tuberculosis*. *Cell Rep* 2013;**5**:1121–31. https://doi.org/10.1016/j.celrep.2013.10.031

108. Bharmal MM, Gega A, Schrader JA-O. A combination of mRNA features influence the efficiency of leaderless mRNA translation initiation. *NAR Genom Bioinform* 2021;**3**:lqab081. https://doi.org/10.1093/nargab/lqab081

109. Mays JN, Camacho-Villasana Y, Garcia-Villegas R *et al*. The mitoribosome-specific protein mS38 is preferentially required for synthesis of cytochrome *c* oxidase subunits. *Nucleic Acids Res* 2019;**47**:5746–60. https://doi.org/10.1093/nar/gkz266